What can Hurricane SAM (2021) tell us about ocean waves under tropical cyclones?

X. Zhao[1,2], L. Oruba[2], D. Hauser[2], B. Zhang[1] and E. Dormy[3]

[1]School of Marine Sciences, Nanjing University of Information Science and Technology, Nanjing, China

[2]Laboratoire Atmosphères, Observations Spatiales (LATMOS), Sorbonne Université, UVSQ, CNRS, Paris, France

[3]Département de Mathématiques et Applications, Ecole Normale Supérieure, CNRS, PSL University, Paris, France

Abstract

We investigate the ocean wave field under Hurricane SAM (2021). Whilst measurements of waves under Tropical Cyclones (TCs) are rare, an unusually large number of quality *in situ* and remote measurements are available in that case. First, we highlight the good consistency between the wave spectra provided by the Surface Waves Investigation and Monitoring (SWIM) instrument onboard the China-France Oceanography Satellite (CFOSAT), the *in situ* spectra measured by National Data Buoy Center (NDBC) buoys, and a saildrone. The impact of strong rains on SWIM spectra is then further investigated. We show that whereas the rain definitely affects the normalized radar cross section, both the innovative technology (beam rotating scanning geometry) and the post-processing processes applied to retrieve the 2D wave spectra ensure a good quality of the resulting wave spectra, even in heavy rain conditions. On this basis, the satellite, airborne and *in situ* observations are confronted to the analytical model proposed by Kudryavtsev et al (2015). We show that a trapped wave mechanism may be invoked to explain the large significant wave height observed in the right front quadrant of Hurricane SAM.

Keypoints

- We take advantage of the unusually large number of observations in Hurricane SAM (2021) to study the physics of waves under a hurricane.
- The innovative CFOSAT-SWIM instrument provides 2D wave spectra which are reliable despite the heavy rain conditions in hurricanes.
- The trapped wave mechanism, or extended fetch, senario can be successfully compared with observations by a saildrone and a NDBC buoy.

Plain Language Summary

Wave measurements in Tropical Cyclones (TCs) can be performed by radars onboard satellites or aircrafts, and by *in situ* devices such as buoys or saildrones. In 2021, a saildrone sailed in Hurricane SAM, providing the first video images of extreme weather in a hurricane, as well as wind and wave measurements. Hurricane SAM was also monitored by the Surface Waves Investigation and Monitoring (SWIM) instrument onboard the China-France Oceanography Satellite (CFOSAT), which measures the wave energy distribution. We explain why these measurements are reliable, despite the heavy rain conditions. Using the saildrone measurements, we also show that the large waves observed in Hurricane SAM may result from the so-called trapped wave mechanism, whereby waves traveling at a velocity similar to the TC displacement can undergo a phenomenal growth.

1 Introduction

Ocean wave measurements under Tropical Cyclones (TCs) are essential to improve our understanding of the generation of waves by TCs. They are unfortunately relatively rare and the reliability of the few existing measurements is often questioned because of the extreme wind and rain conditions inside TCs.

Gravity waves induced by the wind blowing at the surface of the ocean can be measured by *in situ* devices or by radars onboard aircrafts or satellites. The network of the National Data Buoy Center (NDBC) provides measurements of the Significant Wave Height (SWH), their wavelength and

their direction of propagation, as well as measurements of the surface wind. They are a valuable part of the US hurricane warning system and also provide precious observations for research. In 2021, the National Oceanic and Atmospheric Administration (NOAA) and the Saildrone US company have deployed 5 explorer uncrewed surface vehicles designed to make measurements of physical parameters, including waves, within hurricanes, between July and October 2021. On 30 September, one of the saildrones (SDs), SD 1045, crossed Hurricane SAM, on which the present paper is focused, and provided the first video of extreme conditions in a major hurricane.

Since 2019, the Chinese-French Oceanography SATellite (CFOSAT) provides directional wave spectra at the global scale thanks to a rotating multi-beam radar called SWIM (Surface Waves Investigation and Monitoring). These spectra cover the wavelength range $[70 - 500]$ m, giving access to both the wind-sea and the swell waves (Hauser et al., 2021). So far, wave measurements were performed by satellite radar altimeters, providing a global coverage of significant wave height, and by Synthetic Aperture Radars (SAR) onboard satellites (e.g. Sentinel), providing two-dimensional spectra. These spectra are however limited by the so-called azimuth cut-off effect which prevents measurements of the wind sea waves or short swell propagating in directions close to the azimuth direction (see Hauser et al., 2023, for a review). The CFOSAT-SWIM provides an unprecedented detailed description of the waves, offering a chance to measure the wind sea waves. A finer estimate of these waves is crucial for the investigation of wind-waves generated by extreme events like TCs (e.g. Oruba et al., 2022). The CFOSAT satellite also carries a SCATterometer (CSCAT) providing surface wind measurements, collocated with the wave measurements by SWIM. Since 2008, directional wave spectra are also provided by the NOAA Wide Swath Radar Altimeter (WSRA) aboard hurricane reconnaissance aircrafts. Several reconnaissance flights were operated by the NOAA in the case of Hurricane SAM.

The impact of rain on satellite wind and wave products is a major issue. The electromagnetic waves are attenuated and scattered by the atmosphere, mainly due to the presence of water vapor and liquid water (clouds and rain), high frequencies (X-Ku-K-Ka bands) being more impacted than low frequencies (C-S-L bands). Moreover, raindrops impinging onto the sea surface can generate ring waves and turbulence, thus altering the surface roughness. It has been shown by Quilfen et al. (2006) (see also Quilfen et al., 2010) that reliable estimates of SWH, wind speed and rain rate can be obtained in tropical cyclones, thanks to dual-frequency altimeters, operating in both C and

Ku band microwave frequencies. Concerning SAR observations in C-band, Alpers et al. (2016) have shown the important and complex impact of rain on the normalized radar cross sections at medium incidence, whereas Zhao et al. (2021) have analyzed more specifically the impact of rain on wave spectra retrieved in tropical cyclones. The results of Zhao et al. (2021) show an important impact of rain on the accuracy of the retrieved SWH at all the studied incidences (from about 20° to about 50°). They also show that due to the rain impact, the shape of the wave spectra estimated from observations at medium incidence angles (around 40°) depart significantly from their reference spectra.

The rain impact on SWIM measurements (performed in the Ku band) has, so far, not been investigated. However, SWIM products have been used in several studies on the wave field in TCs. Among them, Yurovskaya et al. (2022) analysed the tropical cyclone Goni (2020) by combining multi-satellite observations (including SWIM wave spectra) and a 2D parametric wave model. Other studies are based on a statistical approach, using data over one to several years at the global scale. Xiang et al. (2022) performed a quantitative comparison of the SWIM and CSCAT measurements in TCs to other satellite measurements and model outputs, whereas Shi et al. (2021) and Le Merle et al. (2022) investigated the wave distribution in TCs. Shi et al. (2021) highlighted the SWH asymmetry in TCs, with the highest waves on the right of the TC track in the North Hemisphere (on the left in the South one). The SWH's asymmetry was also shown to mainly depend on the TC intensity, with a decreasing SWH's asymmetry as the TC intensifies. Using 3 years of SWIM data in the North Hemisphere, Le Merle et al. (2022) performed an analysis of the wave characteristics in 67 TCs, by classifying them in three categories (slow, moderate and fast speed), depending on the ratio between the maximum sustained wind and the displacement velocity. The highest SWH were found in the left-front quadrant for slow-moving TCs, in the right-front quadrant for moderate speed TCs and in the right rear quadrant for fast-moving TCs.

Beyond these recent studies involving the SWIM wave spectra, the wave field in TCs, and in particular its asymmetry, has been investigated in many previous studies (see Young, 2017, for a review). The SWH's asymmetry partly results from the asymmetry of the wind field. However, an other source of asymmetry, identified in previous studies as extended fetch or trapped fetch (e.g. Young, 1988; Bowyer & MacAfee, 2005), can also be at stake. In the right quadrants, waves are indeed subject to high wind forcing conditions

for longer periods than usual, because of the translation of the TC: because they move forward with the TC, they experience an extended fetch. The translation speed of the TC plays a critical role in such a wave containment. On the contrary, waves in the left quadrants propagate southward, opposite to the cyclone motion: in this quadrant, the motion of the TC tends to reduce the fetch duration. A one-dimensional analytical model for wave field evolution forced by wind in the right and left quadrants of a moving TC has been proposed by Kudryavtsev et al. (2015). This analytical model (hereafter KGC15 model) is an extension of the self-similarity theory for wave growth (e.g. Badulin et al., 2007) to a moving frame of reference: that of the TC. In the KGC15 model, the wind blows along the direction parallel to the TC axis with a constant speed and generates waves propagating along the same direction. It has been recently extended to a numerical Lagrangian model of the evolution of wave properties along wave rays propagating in TC varying wind fields (Kudryavtsev et al., 2021a,b). Understanding the wave distribution in TCs is still an open issue. In the present paper, the existence of trapped waves in hurricane SAM will be investigated using observational data.

This paper is a multi-data sources investigation of Hurricane SAM, a category 4 major hurricane formed on 22 September 2021 and dissipated on 7 October 2021, with maximum sustained winds of 70 $m.s^{-1}$. Our study is based on satellite, airborne and *in situ* measurements, including NDBC buoys and a saildrone which crossed SAM while it was in category 4. To the best of our knowledge, this is the first time the wave measurements in a TC by a saildrone are used in this context. The datasets and the methods are detailed in Section 2. A detailed comparison of SWIM wave spectra and *in situ* observations in SAM as well as in 8 other hurricanes and tropical storms is then undertaken in Section 3.2. Section 4 aims at demonstrating why despite the heavy rain conditions in TCs, the SWIM wave spectra are still reliable in TCs. On the basis of that work, the existence of trapped waves in SAM is put to the test in Section 5. The results are discussed in Section 6.

2 Datasets and methods

The parameters of tropical storms and hurricanes are available in the International Best Track Archive for Climate Stewardship (IBTrACS, version 4)

database (Knapp et al 2010). Best track data from the US agency, providing 3-hourly data including locations and maximum sustained wind speed, were used here.

Figure 1 shows the trajectory of SAM between 22 September and 7 October 2021. Its maximum sustained winds were larger than 50 $m \cdot s^{-1}$ (setting it in category 3) between 25 September 09:00 and 3 October 00:00. It strengthened to category 4 (winds larger than 58 $m \cdot s^{-1}$) first between 25 September 18:00 and 27 September 06:00, and then between 28 September 06:00 and 2 October 12:00. The locations of the NDBC buoys and the trajectory of the SD 1045 between 22 September and 7 October are indicated in magenta in Figure 1. A few hours after its first intense phase, the track of SAM passed within 188 km east of the NDBC buoy 41040, whereas during its second intense phase, its passed within 60 km west of the NDBC buoy 41044, 30 km west of the saildrone 1045 and 103 km east of the buoy 41049.

The results presented in Section 3.3 also rely on SWIM and NDBC waves measurements in four tropical storms (Sebastien in 2019, Josephine in 2020, Claudette and Fred in 2021), one hurricane of Category 1 (Isaias in 2020), two hurricanes of Category 2 (Sally in 2020 and Earl in 2022) and one hurricane of Category 4 (Ida in 2021).

2.1 *In situ* observations

The NDBC buoys provide hourly one-dimensional frequency wave spectra typically from 0.03 Hz to 0.40 Hz as well as 5 Fourier coefficients corresponding to the directional energy distribution. Two-directional frequency wave spectra are reconstructed using the Maximum Entropy Estimation (MEM) method (Lygre & Krogstad, 1986). Wave parameters, including the SWH, the dominant wave period and the corresponding direction of propagation, are also provided on an hourly basis. The SD data include only the SWH and the peak period of waves every 30 minutes. Unfortunately, no information about the spectral distribution or the direction of propagation of waves is provided by the SD. NDBC buoys (resp. SD) also provide wind measurements (speed and direction) every 10 minutes (resp. 30 minutes). These measurements are performed at the anemometer height. For a proper comparison with other wind measurements, the corresponding 10 m height winds were retrieved using the correction method proposed by Zieger et al. (2009), assuming a logarithmic marine boundary layer under neutral stability conditions. Note that the winds measured by the SD 1045 during SAM were earlier

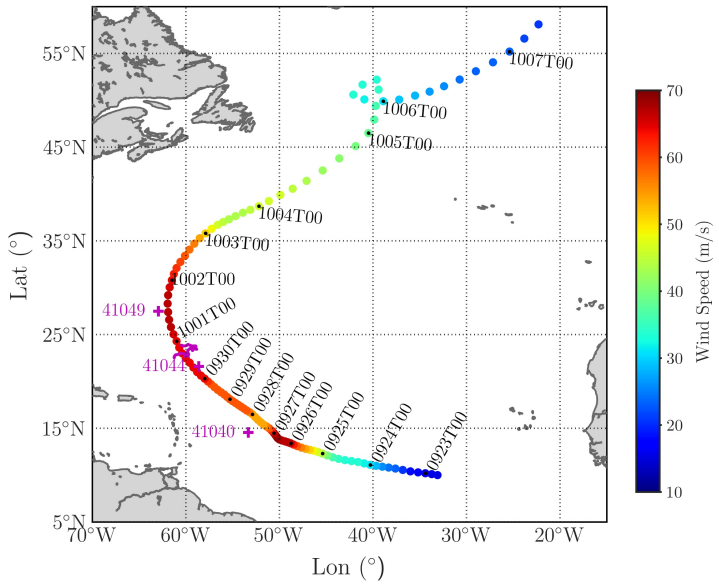

Figure 1: Trajectory of Hurricane SAM between 22 September 2021 and 7 October 2021. Colors: maximum sustained wind speed in $\mathrm{m{\cdot}s^{-1}}$(IBTrACs data). Magenta crosses: location of the NDBC buoys 41040, 41044 and 41049. Magenta line: trajectory of the SD 1045 during the same period.

successfully compared to satellite microwave radiometer measurements and models by Ricciardulli et al. (2022).

2.2 Satellite and airborne wave products

The *in situ* wave measurements were complemented by satellite wave products. CFOSAT has passed several times within SAM, the passage of 1st October 11:32 being of particular interest because it was very close to the TC center (Figure 2a). The nadir beam of SWIM provides SWH measurements (Figure 2b) whereas the 3 off-nadir (or spectral) beams inclined at 6°, 8° and 10° with respect to nadir provide two-dimensional wave slope spectra. In the present study, we use the wave spectra contained in the level 2 (L2) products provided by the CNES Wind and Wave Instrument Center (CWWIC). We mainly use the products derived from the spectral beam at 10°, which tends to be preferred by the community because it is less affected by speckle contamination and wind (Hauser et al., 2021).

The detailed investigation of the impact of rain on SWIM wave spectra carried out in section 4 deserves some details on the geometry and post-processing chain of the SWIM instrument. First, the Normalized Radar Cross Section (NRCS) signals, hereafter denoted as σ_0, are computed within the footprint along the look direction (about 18 km long for the 3 dB footprint) with a high resolution (about 8 m when projected on the surface). Because SWIM is a real-aperture radar, these σ_0 values correspond to signals integrated over the azimuth direction (3 dB footprint of about 18 km). The grey segments shown in Figure 2a show an example of the sampling for successive azimuthal scans of the SWIM. Each grey segment represents the position of the footprint in the elevation direction (the azimuth extension is not represented here). In the post-processing, to avoid conditions of low signal to noise ratio, only the values larger than a threshold value are kept (3 dB above the thermal noise level). The σ_0 signals contain modulations due to the tilt of the long waves when these propagate along the look direction (Hauser et al., 2021). To retrieve the wave information from the σ_0 measurements, a detrending is applied on the σ_0 profiles, and the fluctuation signals, $\delta\sigma_0$, are then calculated. Modulation spectra, hereafter $\mathrm{Pm}(k)$, are then derived from $\delta\sigma_0$ through a Fourier transform, corrected from the speckle noise spectrum and the sensor impulse response spectrum. The modulation spectra are then transformed into wave slope spectra by applying a Modulation Transfer Function (MTF), which involves a renormalization (see

below). The different directions are finally combined to construct a two-dimensional wave slope spectrum at the scale of a box (black rectangles in Figure 2a) of about 70 km $\times$ 90 km, on each side of the nadir track. As explained above, the spectral energy is normalized by using the SWH from the nadir beam. More precisely, the native nadir SWH (dashed blue curve in Figure 2b) is averaged over each box, resulting in the values highlighted by the black squares in Figure 2b and used to normalize the wave spectra. In this averaging process, the values larger than 3 times the standard deviation of the series are deleted. The thus-obtained wave spectra are discretized in 32 wave numbers in the range [0.01–0.28] m^{-1} and 12 directions of propagation, with a 180° ambiguity (see Hauser et al., 2021, for further details). In addition to the L2 products, containing the wave spectra, section 4 also relies on the L1A and L1B products provided by the CWWIC, which contain the σ_0, $\delta\sigma_0$ and Pm variables. An alternative post-processing, involving running averages along the footprints, is proposed by the Ifremer Wind and Wave Operation Center (IWWOC) to build the L2S SWIM products, containing one-dimensional wave slope spectra along the footprints. These data are also used in section 4.

Sentinel 3 has passed twice over SAM: on 30 September 01:34 and on 1st October 01:49. Hence, the present study also involves the 1 Hz averaged L2P SWH and surface wind measurements by the Sar Radar ALtimeter (SRAL) onboard Sentinel 3. Besides, Hurricane SAM was also sampled by the SAR of Sentinel 1. Among the passages of Sentinel 1, the passages on 2 October 09:54 and 3 October 09:45 have retained our interest, because they are very close (both in space and time) to SWIM. The level 2 products of the Sentinel 1a and 1b SAR wave mode were used. They correspond to two-dimensional wave height spectra, built from imagettes of size 20 km $\times$ 20 km, and discretized in 60 wavenumber bins in the range $[0.01, 0.21]$ m^{-1} and 72 directions from 0° to 360°.

Finally, during Hurricane SAM, 4 reconnaissance flights were performed by NOAA. The airborne Wide Swath Radar Altimeter (WSRA), which is a radar altimeter operating at 16 GHz, provides real-time continuous wave measurements. We used the level 4 (L4) product which contains two-dimensional wave spectra $E(k_x, k_y)$ of 65 $\times$ 65 spectral values, where k_x and k_y are the east and north components of the wavenumber vector.

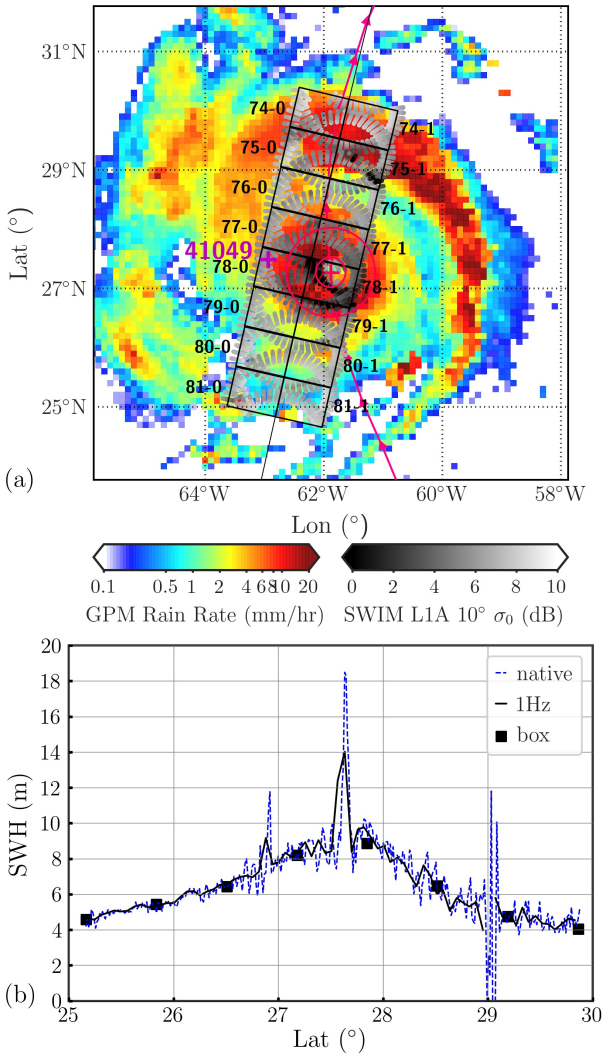

Figure 2: (a) SWIM footprints of the spectral beam at 10° during the passage of SWIM within SAM on 1st October 11:32. Gray color: values of σ_0 (in dB) along the footprints. In black: boxes of the L2 wave products, each side of the nadir track. In colors: rain field (mm/hr) on 1st October 11:30. Red line: trajectory of the center of SAM. Red cross: location of the center of SAM during the passage of SWIM. Red circles: R_{max} and $3\,R_{max}$. Magenta cross: location of buoy 41049. (b) SWH as measured by SWIM along the nadir track: native (dashed blue), 1 Hz averaged (black) and averaged over each box (black squares).

2.3 Wind and rain products

The wave distribution in TCs is partly correlated to the surface wind field. In addition to the wind measurements by the NDBC buoys and the SD, our study also relies on satellite and airborne wind measurements, as well as model outputs. We used the CSCAT L2B wind products of 25-km grid resolution provided by the National Satellite Ocean Application Service (NSOAS). It was recently shown by Zhao et al. (2022) that for high winds (above 15 m/s) and for rain rates up to 6 mm/hr, there is a good agreement between the CSCAT winds and the European Centre for Medium-Range Weather Forecasts (ECMWF) winds. However, it must be kept in mind that they also show that the CSCAT winds retrieved within Typhoon Maysak (2020) are underestimated (compared to ECMWF) for heavy rain conditions (rain rate larger than 6 mm/hr). These data are completed by the surface wind outputs of the ECMWF Integrated Forecasting System (IFS, version 47r1) on a $0.1^\circ \times 0.1^\circ$ grid available every 6 hours. That is worth noting that thanks to a new roughness length parameterization (considering the roughnesslength decrease under extreme wind conditions), the ECMWF IFS numerical simulations in version 47r1 perform much better than the previous versions in capturing the high winds in tropical cyclones (e.g. Bidlot et al., 2020; Li et al., 2021).

The rain rate (hereafter RR) is estimated using the Integrated Multi-satellitE Retrievals for GPM (IMERG) Final Run product. The IMERG product integrates all microwave precipitation estimates from GPM constellation and Infrared-based observations, with Global Precipitation Climatology Centre monthly gauge calibration, including a backward and forward morphing technique (Huffman et al., 2023). The IMERG product in version 7 is half-hourly computed on a $0.1^\circ \times 0.1^\circ$ spatial grid. Only data with a quality index larger than 0.6 are considered in the present study.

2.4 Methods

The natural spectral variable for *in situ* observations being the frequency, the SWIM wave slope spectra $\mathrm{F}(k,\theta)$ (in m^2) are converted to wave height spectra $\mathrm{E}(k,\theta)$ (in m^4) and then to frequency wave spectra $\widetilde{\mathrm{E}}(f,\theta)$ (in $\mathrm{m}^2{\cdot}\mathrm{s}$) using the formula

$$\mathrm{E}(k,\theta) = \frac{\mathrm{F}(k,\theta)}{k^2}\,, \qquad \widetilde{\mathrm{E}}(f,\theta) = \mathrm{E}(k,\theta)k\frac{\mathrm{d}k}{\mathrm{d}f}\,, \tag{1}$$

and the gravity waves dispersion relation. The SWH is estimated as

$$\mathrm{SWH} = 4\sqrt{\mathrm{E}_{tot}} \qquad \text{where} \qquad \mathrm{E}_{tot} = \iint_0^{\pi} \widetilde{\mathrm{E}}(f,\theta)\,\mathrm{d}f\mathrm{d}\theta\,, \tag{2}$$

the double integration being performed over the directions θ and the frequencies f. The dominant frequency, f_p (resp. dominant wavelength λ_p), and the dominant direction, θ_p, provided in the NDBC (resp. SWIM) products have been estimated using different procedures, which prevents from proper comparisons. These parameters are thus recalculated here using the frequency wave spectra $\widetilde{\mathrm{E}}(f,\theta)$. Following Le Merle et al. (2022), a two-dimensional Gaussian filter is applied to the directional spectra to suppress spurious energy peaks that can form at low wavenumbers in the SWIM spectra, before applying the following formula

$$f_p = \frac{\int_{f_{max}-\Delta f}^{f_{max}+\Delta f} f\,\widetilde{\mathrm{E}}(f,\theta_{max})\mathrm{d}f}{\int_{f_{max}-\Delta f}^{f_{max}+\Delta f} \widetilde{\mathrm{E}}(f,\theta_{max})\mathrm{d}f}\,, \qquad \theta_p = \frac{\int_{\theta_{max}-\Delta\theta}^{\theta_{max}+\Delta\theta} \theta\,\widetilde{\mathrm{E}}(f,\theta_{max})\mathrm{d}\theta}{\int_{\theta_{max}-\Delta\theta}^{\theta_{max}+\Delta\theta} \widetilde{\mathrm{E}}(f,\theta_{max})\mathrm{d}\theta}\,, \tag{3}$$

where (f_{max}, θ_{max}) is the location of the maximum energy, and (Δf , $\Delta\theta$) are the frequency and direction intervals. The same procedure was applied to the SAR and WSRA wave height spectra. The direction convention for θ is the direction from which waves travel, measured clockwise from North. The dominant wavelengh λ_p is deduced from f_p using the dispersion relation.

The following study involves distance calculations between SWIM and *in situ* measurements. The fact that the SWH measurements are performed along the nadir track (black line in Figure 2), whereas the wave spectra (hence the λ_p and θ_p parameters) are computed over boxes (black quadrangles in Figure 2), is taken into account when calculating the distance between measurements.

3 Waves observations by SWIM and *in situ* devices

In this section, the *in situ* observations by NDBC buoys and the SD 1045 are used to assess the reliability of the SWIM wave spectra under heavy rain conditions in SAM. In addition, SWIM wave spectra are compared to NDBC wave spectra within 8 other tropical storms and hurricanes.

3.1 Multi-sources composite description of wind and waves conditions in SAM

A composite over 3.5 days is first built, using all of the available observations, in order to characterize the wave distribution in Hurricane SAM. Figure 3 is a composite constructed using different data sources over 3.5 days, between 29 September 00:00 and 2 October 12:00. That period corresponds to the second high-intensity phase of SAM. During that period, its maximum sustained winds were comprised between 59 $m{\cdot}s^{-1}$ and 67 $m{\cdot}s^{-1}$, which corresponds to a relative change in intensity of about 10%. The measurements are all reported in the frame of SAM, with the top of the figure corresponding to the TC propagation direction. The figure presents both waves and winds *in situ* measurements by the 3 NDBC buoys (41040, 41044 and 41049) and by the saildrone SD 1045. The wave measurements by SWIM during 3 passages (on 29 September 22:32, 1st October 11:32 and 2 October 11:16) are superimposed, as well as the SWH as measured by the Sentinel-3 altimeter during the two passages on 30 September 01:34 and 1st October 01:49. The WSRA wave data collected during the reconnaissance flight performed between 29 September 20:38 and 30 September 03:03 are also reported on the same figure. Finally, the CSCAT winds are also plotted in Figure 3d, at the position of the SWIM wave boxes.

Figures 3a, 3b and 3c show the SWH, the dominant wavelength and the dominant wave directions, respectively, whereas Figure 3d shows the wind vectors. In Figure 3c, the 180° ambiguity inherent to the SWIM wave spectra is raised using the CSCAT winds, by assuming that under TCs conditions, the angle between the direction of the wind and the direction of wave propagation is always lower than 180°, which has been observed in many previous studies. The largest waves are observed near the TC center and in the right front quadrant at distances smaller than $3\,R_{max}$ (Figure 3a), whereas the longest wavelengths are observed in the left front and right front quadrants (Figure 3b). Waves in the two front quadrants radiate out of a region to the right of the hurricane center, corresponding to a region of strong wind (see Figures 3d and 5b which shows the CSCAT wind field on 1st October 11:32). It is worth noting that wind and dominant waves are never aligned. The angle between winds and waves is about 60° in the right front quadrant, and larger than 60° in most locations in the other quadrants (compare Figures 3c and 3d).

It is interesting to compare these results to Le Merle et al. (2022). Be-

tween 29 September 00:00 and 2 October 12:00, the displacement velocity V of SAM increased from 3.6 m·s^{-1} to 9.3 m·s^{-1} on 1st October 18:00 before decreasing to 7.7 m·s^{-1}. The ratio between the maximum sustained wind U_{max} and the displacement velocity V was mainly comprised between 5 and 12, which corresponds to a moderate speed TC, according to their classification. The above description is consistent with the results obtained by Le Merle et al. (2022) for moderate speed TCs.

3.2 SWIM and *in situ* estimations of wave parameters in SAM

In order to assess the reliability of SWIM wave measurements in Hurricane SAM, a comparison of the wave parameters as measured by SWIM and by the *in situ* devices is performed. The data provided by the NDBC buoys and by the SD are considered here as the most reliable wave measurements in SAM. The main issue raised when comparing satellite to *in situ* measurements is due to the sparse nature of these two types of data, both in space and time. On the one side, the *in situ* observations are performed at the sole location of the device, which is fixed for the NDBC buoys and which changes over time for the SD, according to its trajectory. These data are provided every 10 minutes for the NDBC buoys (hourly for the spectra) and every 30 minutes for the SD. On the other side, SWIM passages in a given region of the globe take place once or twice a day, and the wave measurements are performed only along the nadir track (for the SWH) and in two bands of about 90 km wide on each side of the track (for the wave spectra). There is therefore inevitably a temporal and spatial difference between the SWIM and *in situ* measurements. Such differences can be critical under TCs because of the inhomogeneous distribution of waves in TCs and because of their temporal variability, due to the wind temporal variations and to the TC displacement. Such comparisons must thus be performed carefully, especially when assessing the quality of satellite measurements.

The brown lines in Figure 4 show the time evolution of the SWH (panels a,d,g,j), the dominant wavelength λ_p (panels b,e,h,k) and the dominant direction θ_p (panels c,f,i) as measured by the buoys 41040 (panels a,b,c), 41044 (panels d,e,f), 41049 (panels g,h,i) and the SD 1045 (panels j,k) between 20 September and 10 October. The parameters λ_p and θ_p are calculated using the method described in Section 2.4. Note that the SD data do not allow

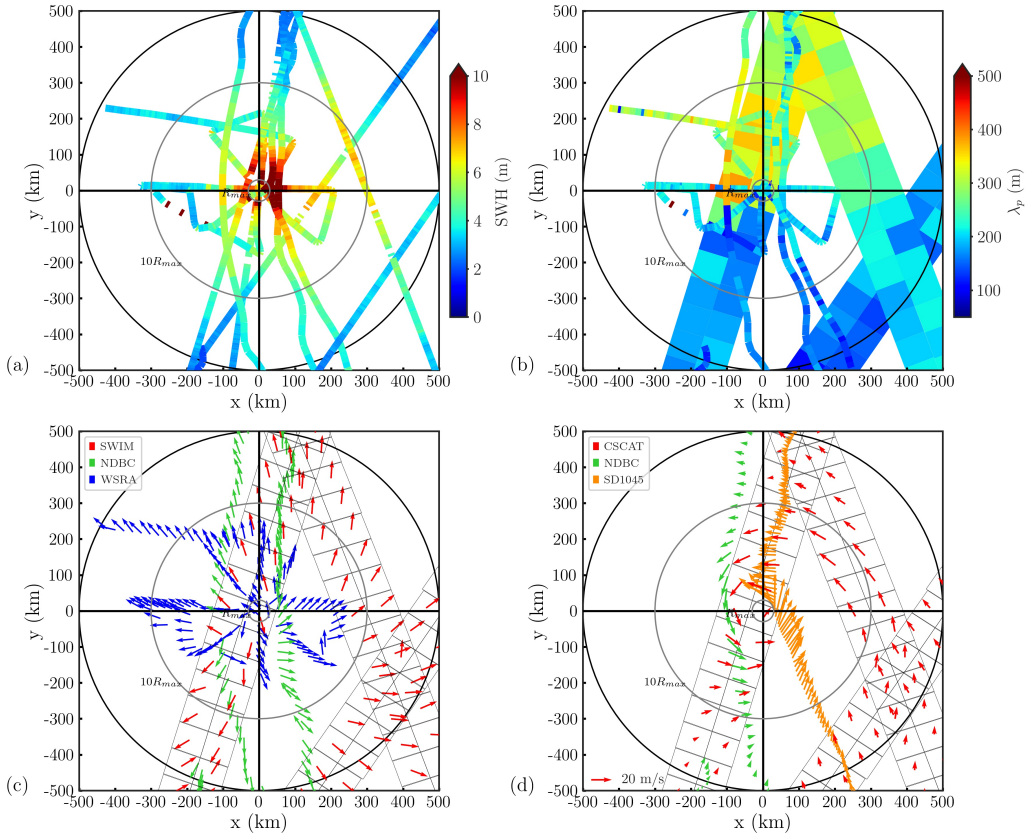

Figure 3: Composite representation of observations between 29 September 00:00 and 2 October 12:00 reported in the frame of Hurricane SAM. (a) SWH from SWIM, Sentinel 3, the airborne WSRA radar, 3 NDBC buoys and the SD, (b) Dominant wavelength λ_p from SWIM (large squares), the airborne WSRA radar, 3 NDBC buoys and the SD, (c) Dominant wave direction from SWIM, the airborne WSRA radar and 3 NDBC buoys (see inset for color code), (d) Wind vectors from CSCAT, 2 NDBC buoys and the SD (see inset for color code). Black circles indicate R_{max}, $10\,R_{max}$ and a radius of 500 km, with $R_{max} = 28$ km.

to derive θ_p. The gray curves correspond to the wind speed measured by the buoys and the SD. We co-localized 40 measurements from SWIM, by allowing a maximum distance of 300 km between the SWIM boxes and the *in situ* devices, and a maximum time-lapse of 30 minutes for the buoys and of 15 minutes for the SD. The wave parameters derived from the SWIM wave spectra are superimposed as black circles in Figure 4. In Figures 4c,f,i, the 180° ambiguity on SWIM spectra was raised by selecting the direction closest to that measured by the buoy.

Among the *in situ* devices, the buoy 41040 is the farthest one from the TC track (see Figure 1), at 188 km west of the TC track: during the passage of SAM, it measured a SWH of 4.1 m on 27 September 06:40 (panel a). The largest SWH is measured by the SD (panel j): on 30 September 15:00, while it was located at 39 km north-east of the TC track, it measured a SWH of 14.2 m. Going back 6.3 hours earlier, the buoy 41044 measured a SWH of 12.2 m, 60 km east of the TC track (panel d). The track of SAM goes further from the buoy 41049, located west of the track at a distance of 103 km (see also Figure 1): a SWH of 6.7 m is measured by the buoy 41049 on 1st October 11:40 (panel g). There is an almost simultaneous occurrence between the maximum of SWH and the maximum wind speed as measured by the buoys 41044, 41049 and by the SD resp., with maximum wind speeds of 24.4 $\mathrm{m{\cdot}s^{-1}}$, 34.6 $\mathrm{m{\cdot}s^{-1}}$ and 43.5 $\mathrm{m{\cdot}s^{-1}}$ resp. (see panels d, g and j). The value of SWH corresponding to the closest measurement by SWIM during its passage on 1st October 11:32 is 8.2 m (panel g). Unfortunately, there was no passage of SWIM in the vinicity of the buoy 41044 and of the SD between 28 September 22:46 and 2nd October 11:18: both SWH peaks on panels d and j are thus not sampled by SWIM.

During the passage of SWIM close to the buoys 41044, 41049 and to the SD, the dominant wavelength undergoes a sharp decrease from larger values to smaller values concomitant with the maximum of wind and SWH: in a few hours on 30 September, it decreases from 250 m to 150 m for the buoy 41044 (panel e) and from 300 m to 100 m for the SD (panel k) and on 1st October from 400 m to 100 m for the buoy 41049 (panel h). This result is consistent with Figure 3b: the *in situ* devices, first undergo the longest waves, in the front quadrants of SAM, before undergoing shorter waves in the rear quadrants. The direction of propagation of waves also undergoes an abrupt change during the passage of SAM synchronised with the maximum wind and SWH (panels f and i): the buoys 41044 and 41049 first measure waves propagating forward and then waves propagating rather backward, which is

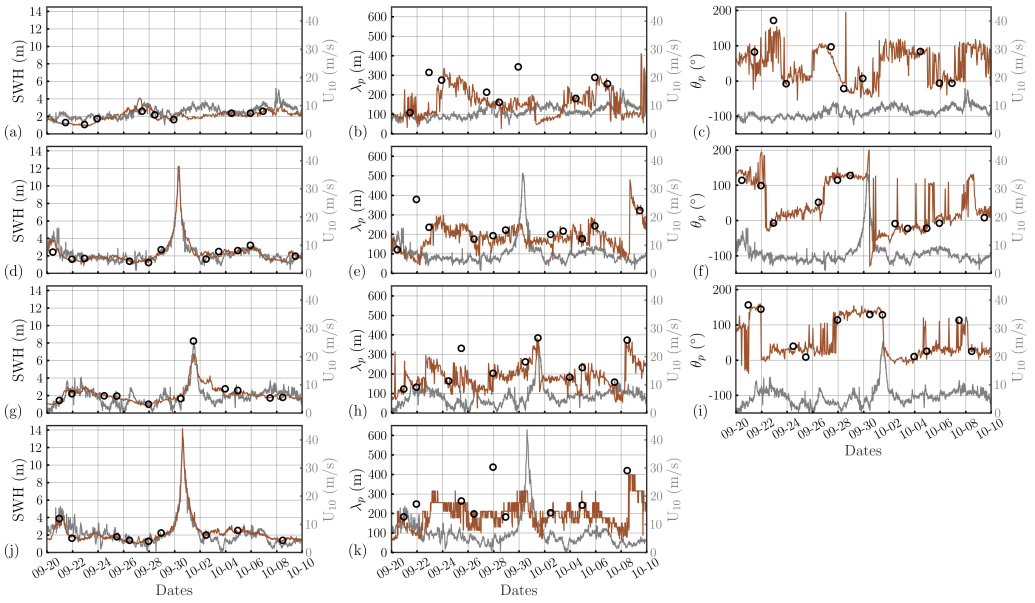

Figure 4: Brown curves: SWH (panels a,d,g,j), dominant wavelength λ_p (panels b,e,h,k) and dominant direction θ_p (panels c,f,i) as measured by the buoys 41040 (panels a,b,c), 41044 (panels d,e,f), 41049 (panels g,h,i) and the SD 1045 (panels j,k) between 20 September and 10 October. Gray curves: wind speed. Black circles: closest SWIM measurements.

consistent with Figure 3c.

The comparison of wave characteristics between SWIM measurements and *in situ* observations over the period shown in Figure 4 exhibits overall consistency. The discrepancy between the SWIM and *in situ* SWH is of order 10% and does not exceed 30%. The few cases where the difference in the peak values is significant correspond either to multi-modal systems with different wavelengths and directions but comparable energies, or to low SWH cases (SWH $\simeq$ 1 m) where SWIM wave measurements are known to be less reliable.

3.3 Two-dimensional wave spectra in heavy rain

During the entire period subject to investigation here, the passage of SWIM within SAM on 1st October 11:32, very close to the buoy 41049, corresponds to heavy rain along the SWIM track. In the following, we will focus on

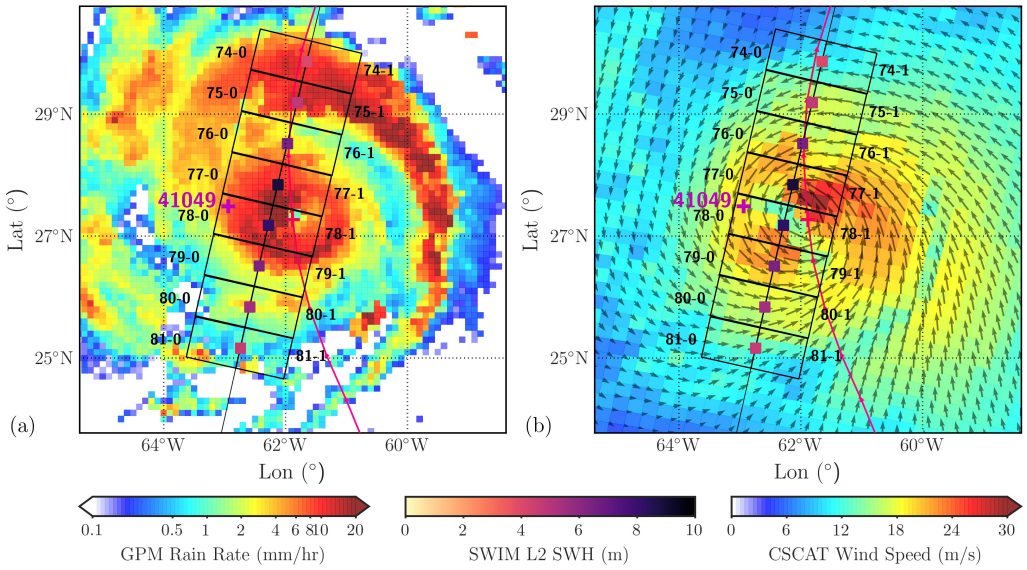

Figure 5: SWIM nadir track (black line) and boxes (black quadrangles) during the passage of SWIM within SAM on 1st October 11:32, close to the buoy 41049 (magenta cross). (a) Rain rate field (in mm/hr) on 1st October 11:30 and (b) surface wind field from CSCAT (colors: intensity in m/s, arrows: directions). Colored squares: nadir SWH averaged over boxes. Red line: trajectory of the center of SAM. Red cross: location of the center of SAM during the passage of SWIM.

this track. Figure 5 shows the nadir track and the boxes over which the wave spectra are computed, superimposed to the rain rate field at 11:30 (Figure 5a) and to the wind field as measured by CSCAT (Figure 5b). The boxes numbered as 77-0, 77-1, 78-0 and 78-1 are the most severely affected by rain, with the rain rate exceeding 20 mm/hr in some areas of these boxes (Figure 5a). The wind speed from CSCAT does not exceed 30 $\mathrm{m{\cdot}s^{-1}}$, which is largely underestimated, roughly by a factor of 2 compared to the IBTrACS estimation. Note that such saturation is not specific to CSCAT: it is known that at high wind speeds (winds larger than 30 $\mathrm{m{\cdot}s^{-1}}$), wind information from scatterometers saturates.

To assess for the reliability of SWIM wave spectra under rain conditions, the wave height spectrum of box 78-0 is compared to that of the buoy 41049, with the distance between the center of the box and the buoy being 33 km and

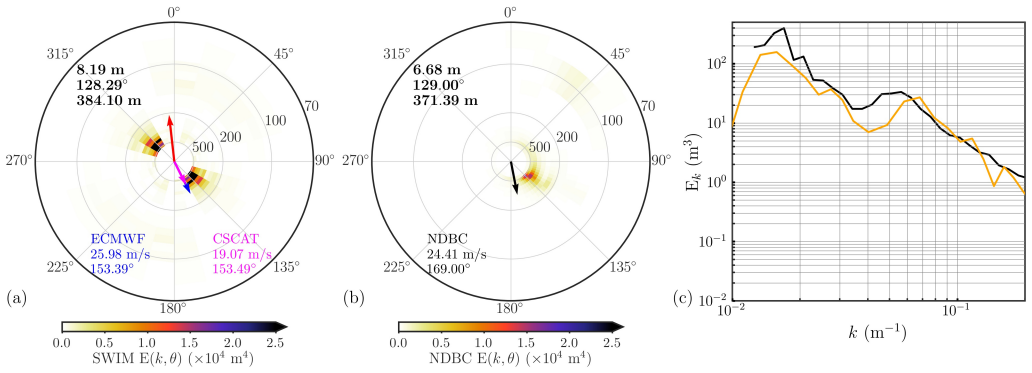

Figure 6: Two-dimensional wave height spectra $\mathrm{E}(k,\theta)$ measured (a) by SWIM in box 78-0 (10° beam) on 1st October 11:32 and (b) by the NDBC buoy 41049 on 1st October 11:40. Arrows: wind vectors. (c): Corresponding SWIM (black) and NDBC (orange color) omni-directional wave spectra $\mathrm{E}_k(k)$.

the time-lapse being only 8 minutes. These are the closest SWIM and *in situ* measurements available within TC SAM. The wave height spectra are shown in Figure 6. Both two-dimensional spectra shown in Figures 6a,b exhibit a dominant wave system characterized by a similar dominant wavelength (384 m for SWIM and 370 m for the buoy) coming from the south-east, with $\theta_p \approx 129°$ (with a 180° ambiguity for SWIM). However, the SWIM SWH (8.2 m) is overestimated by about 20% compared to the buoy SWH. Either the rain or the fact that the box is closer to the centre of the cyclone by about 30 km compared to the buoy could explain this discrepancy. The omni-directional spectra $\mathrm{E}_k(k)$ (in m^3), constructed as

$$\mathrm{E}_k = \int_\theta \mathrm{E}(k,\theta)\, k \,\mathrm{d}\theta\,, \tag{4}$$

are shown in Figure 6c. Both profiles are comparable although the energy measured by SWIM at wavelengths larger than 100 m is larger than that measured by the buoy. A secondary wave system coming from the northeast is detected by both instruments, at a wavelength of 125 m according to SWIM and 100 m according to the NDBC buoy.

In the case of SAM, there are unfortunately no other such close comparisons of satellite and *in situ* measurements under high rainfall rates. In addition to SAM, we however also identified 8 tropical storms and hurricanes

from 2019 to 2022 for which collocated SWIM and NDBC wave spectra close to the storm center are available, allowing a maximal distance between the box center and the buoy of 70 km. The 2D and 1D wave height spectra are shown in Figures 7 and 8 (they are ranked from largest to lowest SWH as measured by SWIM). The maximum rain rate in the SWIM boxes varies between 0.2 mm/hr and 48.5 mm/hr. Even in the strongest rain cases (first and second row in Figure 7, second row in Figure 8), there is a good consistency between SWIM and *in situ* wave spectra, with the wave parameters differing by less than 20%. The SWIM and *in situ* 1D spectra are similar in the peak energy region and for larger values of wavenumber. However, they differ significantly at wave numbers lower than k_p. Indeed, SWIM is known to overestimate energy at small wave numbers, especially for SWH less than about 3 meters (e.g. Jiang et al., 2022). This effect is clearly visible in the last two spectra shown in Figure 7 and in the four spectra in Figure 8. In the first case of Figure 7 (SWH larger than 6 m), we expect this effect to be less pronounced. A similar analysis to that conducted in section 4 was carried out: the energy measured by SWIM at low wavenumbers does not appear to be related to rainfall. This case actually corresponds to measurements very close to the center of the cyclone (see Figure 7a) where spatial variability is significant, which could explain the discrepancy between the SWIM and *in situ* spectra at low wavenumbers. Another possible explanation could be related to the choice of the cut-off frequency in the post-processing of data acquired by the NDBC buoy, which may attenuate the energy measured at low wavenumbers.

The results shown in this section exhibit overall consistency between the SWIM and *in situ* measurements of wave parameters and wave spectra in the wave energy containing part (although some artefacts seem to appear at wavenumbers much lower than the peak of the spectra), even in the presence of heavy rain. Note that the SAR wave spectra acquired in cyclones are more challenging to use. Indeed, these spectra are impacted by the azimuth cut-off effect, which prevents measurements of the wind sea waves or short swell. The cut-off is particularly important for wave energy propagating in directions close to the SAR azimuth direction. This is highlighted in A where co-located SWIM and SAR spectra measured within Hurricane SAM are compared (see Figure 16 in A). Finally, we identified some cases in moderate to heavy rain conditions, where the SAR spectra exhibit a strong attenuation compared to SWIM, which can not be attributed to the cut-off effect (because corresponding to waves propagating in a direction closer to the range than

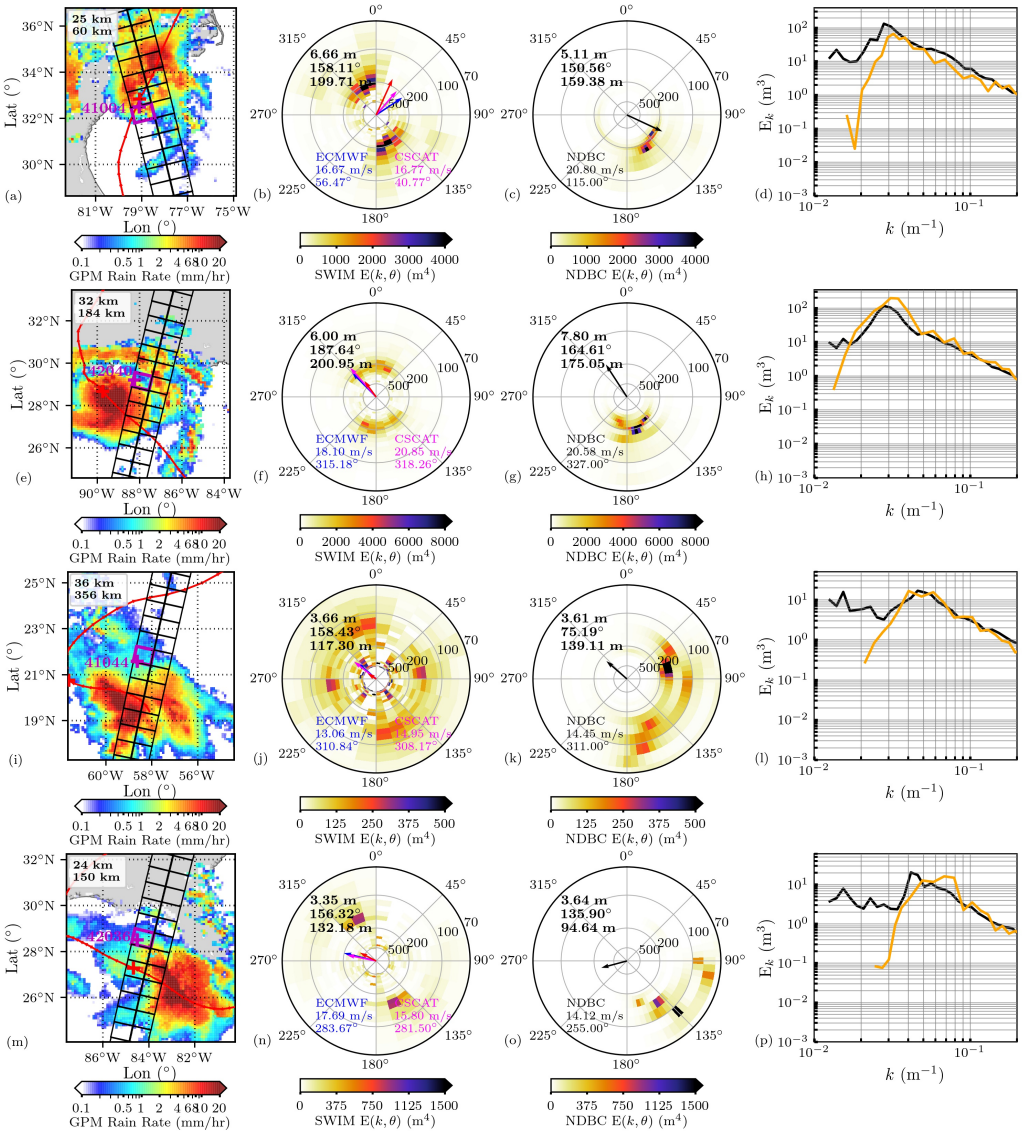

Figure 7: First column: SWIM boxes (black quadrangles) superimposed to the rain rate field in mm/hr (in colors); red line: the best track of the storm; red cross: storm center during the passage of SWIM; magenta cross: NDBC buoy; white box: SWIM-buoy distance and SWIM-TC distance. Second column: SWIM wave height spectrum (closest box to the NDBC buoy, highlighted in magenta in the first column). Third column: NDBC wave height spectrum. Fourth column: 1D wave height spectra. Same as Figure 6 but for hurricanes Isaias (first row), Ida (second row), tropical storm Sebastien (third row) and hurricane Sally (fourth row).

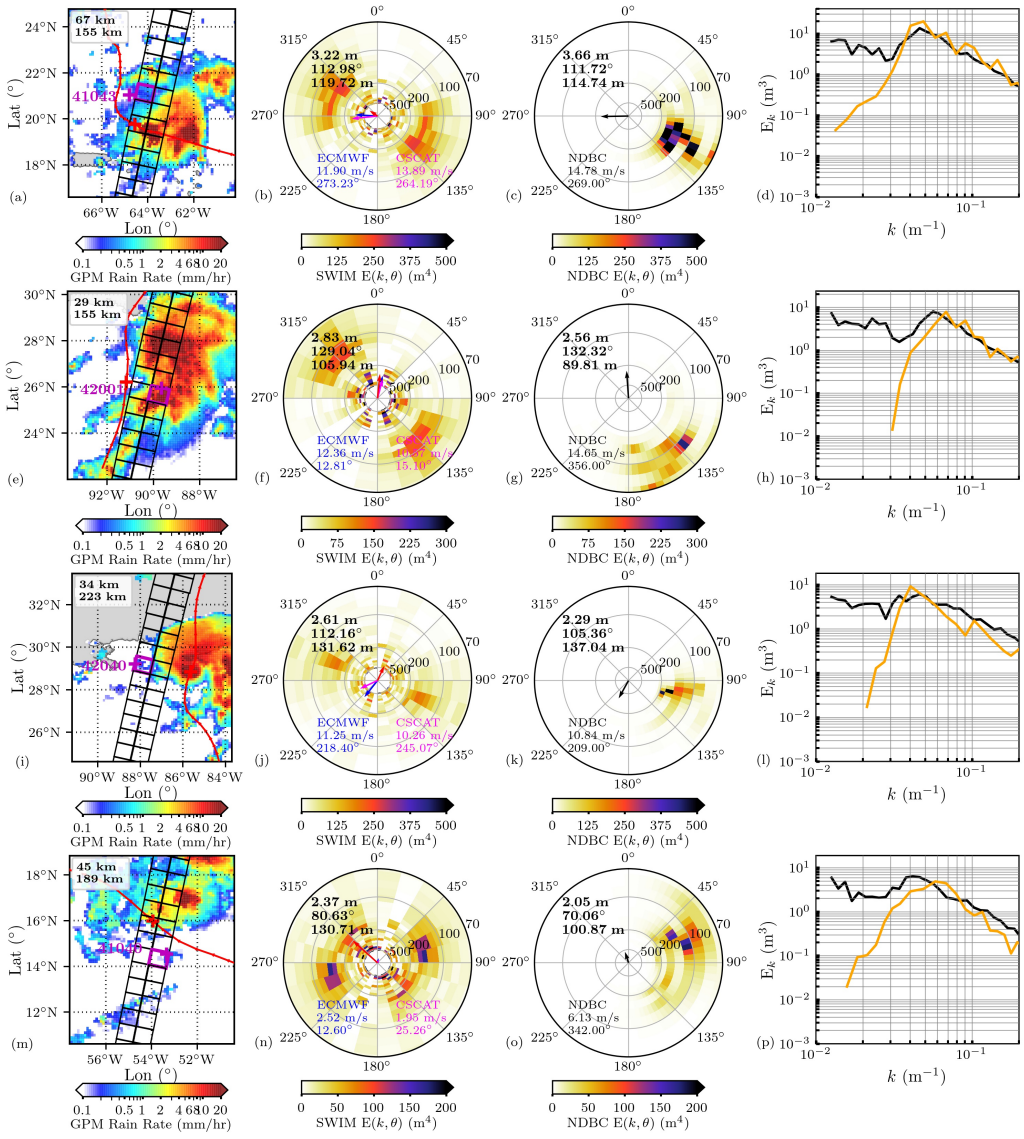

Figure 8: Same as Figure 7, for hurricane Earl (first row) and tropical storms Claudette (second row), Fred (third row) and Josephine (fourth row).

to the azimuth direction) and which suggest that the spectra resulting from the 2D SAR imagettes are more strongly affected by rain than the 1D SWIM footprints (see Figure 17 in A).

4 Rain impact on SWIM wave spectra

The aim of this section is to understand why the SWIM wave spectra seem reliable, even in heavy rain conditions. To do so, we focus on the passage on 1st October 2021 11:32 during hurricane SAM. The footprints corresponding to the spectral beam at 10° within 350 km from the TC center are shown in Figure 2a.

4.1 Rain impact on SWIM radar signals

We first focus on three footprints, one in light rain (1.1 mm/hr), the other one in moderate rain (9.4 mm/hr) and the third one in heavy rain (24.6 mm/hr). In following, they are denoted as cases 1, 2 and 3 respectively. The location of the footprint in the rain rate field is highlighted in Figures 9a, 10a and 11a, whereas the σ_0 profile with incidence along the footprint is shown in Figures 9b, 10b and 11b. The signal is attenuated by rain in cases 2 and 3, with the attenuation reaching 12 dB at the incidence of 11° in case 3 compared to case 1. Note that the parts of the signal which are too attenuated are filtered in the post-processing. The threshold profile corresponds to the dashed red curve in Figures 9b, 10b and 11b. Whereas the signal-to-noise ratio is high in case 1, at the far range of the footprint, the signal is close to noise in case 2 and below noise in case 3. As far as a significant part of the signal is larger than the threshold, the post-treatment can be conducted. For example in case 3, the signal used as input to the wave analysis will be limited to the $9 - 10.5°$ range in incidence, whereas in case 1, all values in the range $9 - 11°$ will be kept in the analysis. In case 2, the far range will be limited to about 10.8°.

Additionally, rain inhomogeneities within the footprints can cause distortion of σ_0. This is particularly visible in case 2 (Figure 10b) where σ_0 exhibits large-scale oscillations at a scale of the order of the swath length (about 20 km for beam 10°), much larger than 500 m. The standard deviation of the σ_0 profile around its mean value, after filtering by a low pass filter (filtering of length scales under 500 m, associated to waves) allows to quantify

the large-scale variability within the footprint. Its value, denoted as $lsvar$, is indicated in the captions of Figures 9, 10 and 11: rain inhomogeneities within the footprints, causing large-scale oscillations of the σ_0 profile, result in larger values of $lsvar$. The signal fluctuations $\delta\sigma_0$ in the L1B product, derived from σ_0 by subtracting the mean trend, are shown in Figures 9c, 10c and 11c. As expected, they also exhibit large-scale oscillations due to rain inhomogeneities in cases 2 and 3.

The resulting modulation spectra, $\mathrm{Pm}(k)$, contained in the L1B (resp. L2S) products are shown in Figures 9d, 10d and 11d in blue (resp. orange) color lines: the large-scale oscillations of $\delta\sigma_0$ in cases 2 and 3 yield a peak of energy in the modulation spectra at small k in Figures 10d and 11d. It is worth noting that the peak at small k is smaller in the L2S modulation spectra than in the L1B modulation spectra. Indeed, the L2S modulation spectra result from the Welch method (Welch, 1967) where the σ_0 values are splitted in 15 overlapping windows before being used as input of 15 fast Fourier transforms (FFT) whose spectral energy is then averaged to build the modulation spectrum. Such a process logically reduces the impact of the inhomogeneity of rain along the footprint. In contrast, in the L1B processing, the full length of the σ_0 samples is used as input to the FFT, which leads to more noisy modulation spectra, while the averaging is carried out in the spectral space during the construction of the two-dimensional wave slope spectrum, after filtering the low wavenumber components ($k < k_{min} = 0.01$ m^{-1}). Hence, the comparison of L1B and L2S modulation spectra corroborates the correlation between the large-scale oscillations of σ_0 and $\delta\sigma_0$ (as well as the resulting peak in the modulation spectrum at small k) and rain inhomogeneities along the footprint.

The above conclusions have been statistically verified using all the footprints within 350 km from the TC center during the passage of SWIM on 1st October 2021 (see B). In B, using SWIM 10° and 8° beams, we also show that rain mainly impacts the L1B modulation spectra at small wavenumbers (wavelenghs larger than 1 km), rather than the waves range ($[70 - 500]$ m). A similar study was conducted for the rainiest cases shown in Figures 7 and 8, leading to the same conclusions.

4.2 Rain impact on L2 SWIM wave slope spectra

The L2 (resp. L2S) wave slope spectra corresponding to the L1B (resp. L2S) modulation spectra are superimposed in Figures 9d, 10d and 11d, in green

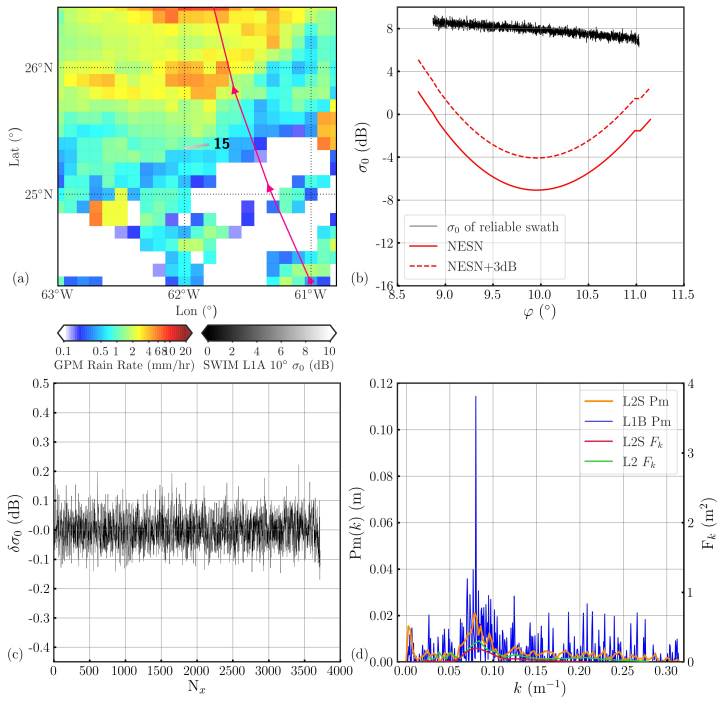

Figure 9: Case of light rain (1.1 mm/hr): box 80-1, swath 15, $lsvar = 0.0284$, $\phi = 80°$. (a) Rain rate field (colors) superimposed to the footprint. Dashed: σ_0 values along the footprint. (b) Black: reliable σ_0 profile (in dB) as a function of the incidence angle. Solid red: noise equivalent σ_0. Dashed red: noise equivalent σ_0 + 3 dB. (c) Fluctuation signal $\delta\sigma_0$ profile (in dB). (d) L1B (blue) and L2S (orange) modulation spectra superimposed to L2 (green) and L2S wave slope spectra.

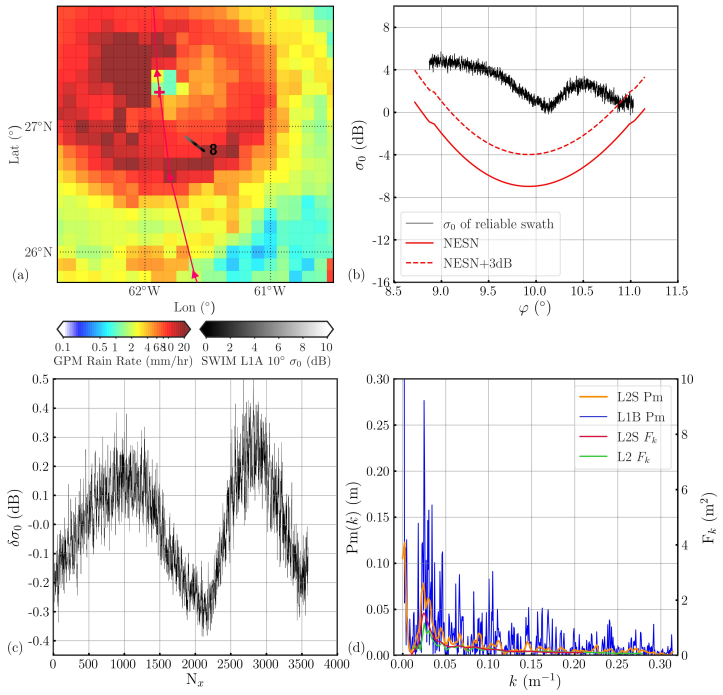

Figure 10: Same as Figure 9 but in a case of moderate rain (9.4 mm/hr): box 78-1, swath 8, $lsvar = 0.784$, $\phi = 131°$.

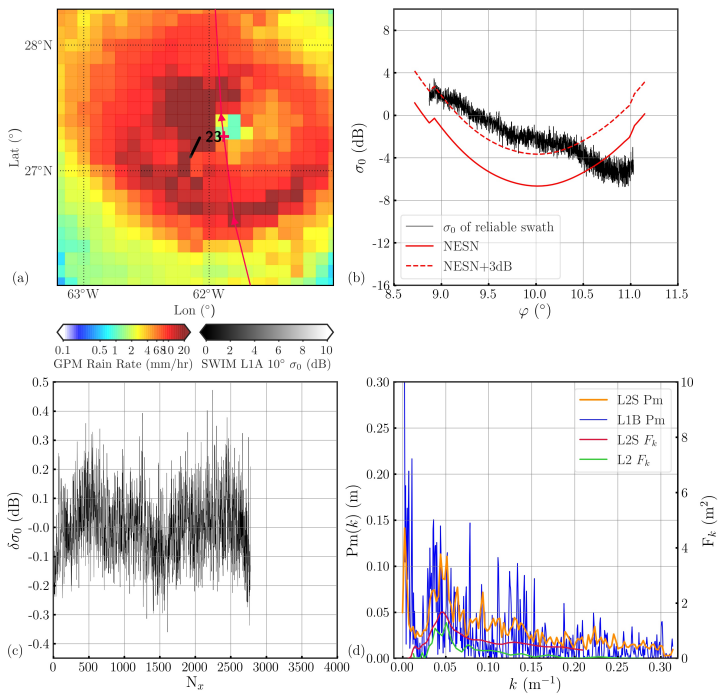

Figure 11: Same as Figure 9 but in a case of heavy rain (24.6 mm/hr): box 78-1, swath 23, $lsvar = 0.364$, $\phi = 23°$.

(resp. red) color lines. They also exhibit a peak of energy corresponding to the waves propagating in the azimuth direction. However, in cases 2 and 3, they do not exhibit any peak at small wavenumbers, contrary to the modulation spectra. In the post-processing, values corresponding to wavenumbers smaller than $k_{min} = 0.01$ m^{-1} are indeed filtered. Hence, the peak in the modulation spectra at small k due to the large-scale oscillations of σ_0 does not affect the wave slope spectra.

As explained in section 2, the L2 two-dimensional wave slope spectra at the scale of a box are reconstructed by combining the measurements within the footprints contained in the box. Figure 12 gathers the averaged parameters of the 25 footprints of the 10° beam in box 78-1 (see Figure 20a). The averaged $\overline{\sigma_0}$ is most attenuated around the 30° and 190° directions, which are characterized by the highest rain rates; this results in large values of the $lsvar$ parameter in these directions. The energy of waves in the modulation spectrum is quantified by $\mathcal{E}_{k>k_c}$ (defined in (5), with $k_c = 2\pi \cdot 10^{-3}$ m^{-1}): it indicates that the dominant direction of waves lies around 150°. The dominant waves are thus detected by footprints undergoing moderate rain. Generally speaking, it is worth noting that because of the different locations of the footprints in the rain field, different situations are possible. In the configuration where the dominant waves direction coincides with footprints undergoing light or no rain (i.e. the footprints in stronger rain correspond to directions of low energy wave), the rain is not expected to affect the wave spectra, since the wave energy is measured by footprints in light or no rain. In other configurations, where the footprints measuring wave energy undergo moderate or heavy rain (like in Figure 12), we have shown in this section that as long as the attenuation is not too important, the wave spectra remain reliable.

It is important to note that the post-processing leading to the L2 wave slope spectra involves a normalization by the nadir SWH. A detailed study of the impact of rain in the post-processing of nadir measurements is out of the scope of the present paper. However, it can be noted that the comparisons presented in Figures 7 and 8 do not reveal a clear trend regarding the effect of rain on the nadir SWH.

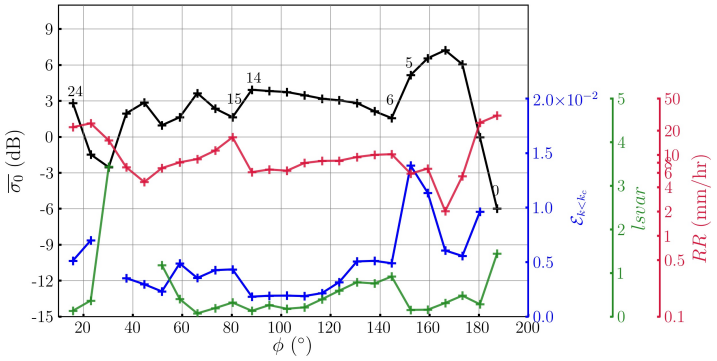

Figure 12: Values of $\overline{\sigma_0}$ (black), RR (red), $lsvar$ parameter (green) and $\mathcal{E}_{k>k_c}$ (blue) as a function of the azimuth direction, corresponding to the 25 footprints of the 10° beam in box 78-1 (see Figure 20).

5 Wave asymmetry in Hurricane SAM

Largest waves are found in the right front quadrant of TCs, as highlighted in Figure 3a for SAM. The asymmetry in the wave field may simply originate from the asymmetry in the wind field (highlighted in Figures 3d and 5b), or may be due to the so-called extended fetch effect (Young, 1988). The aim of this section is to take advantage of the many measurements available in Hurricane SAM to investigate the physical origin of the wave asymmetry.

The 'extended fetch' idea has been recently formalised under simplifying assumptions by Kudryavtsev et al. (2015) here referred to as the KGC15 model, see also C. Note that this analytical model has been further extended to a numerical model (Kudryavtsev et al., 2021a,b). We use here the analytical version of this work, i.e. that of Kudryavtsev et al. (2015).

The observational data for SWH shown in Figure 3a are first compared to the SWH as predicted by the KGC15 model. The latter are calculated by combining (7), (8) and (9) in C. For this calculation, we use the surface wind speed measured by the buoys, the SD, the CSCAT instrument and the Sentinel 3-SRAL, as well as the ECMWF surface wind speed interpolated along the aircraft trajectory. In order to facilitate the comparison, the SWH observations are reported in Figure 13a, whereas the SWH predicted by the KGC15 model are juxtaposed in Figure 13b. The figure is presented in the reference frame of the TC and orientated with the TC propagation direction upward. Note that the wave properties in gray shaded area cannot be de-

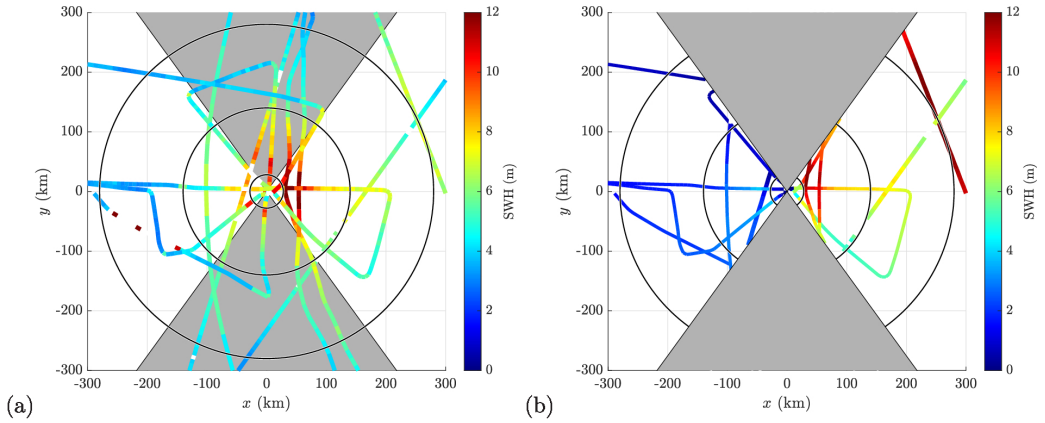

Figure 13: (a) Composite representation of SWH observational data between 29 September 00:00 and 2 October 12:00 reported in the frame of Hurricane SAM. (b) SWH as predicted by the KGC15 model. Shaded gray: area not described by the KGC15 model. Red Black circles indicate R_{max}, $5\,R_{max}$ and $10\,R_{max}$.

scribed by the KGC15 model, because in these areas, the wind vectors are nearly orthogonal to the TC propagation. The model reproduces the asymmetric wave field. In the right quadrants, the modelled SWH is globally consistent with the observed SWH, except on the SWIM track of 2 October, for which the model overestimates the SWH. This could be explained by the large distance of this track from the center of the cyclone (more than $10\,R_{max}$). The model also seems to underestimate the SWH in the left quadrants. It is important to keep in mind that the KGC15 model is based on strong assumptions, including a homogeneous wind field in each of the right and left quadrants. Discrepancies between the model estimations and the observations are therefore inevitable. In particular in the left quadrants the waves in the KGC15 model travel along a direction parallel to the cyclone displacement. No wave energy is radiated from the eyewall in this model. The KGC15 model can however be used to investigate the possible existence of trapped waves in the right quadrants of SAM: this is what we tackle in the following.

Since SWIM measurements are either too far from the center of the cyclone or in the region not covered by the model, they are no longer used in the following. Instead, we first focus on the aircraft passage through the right-

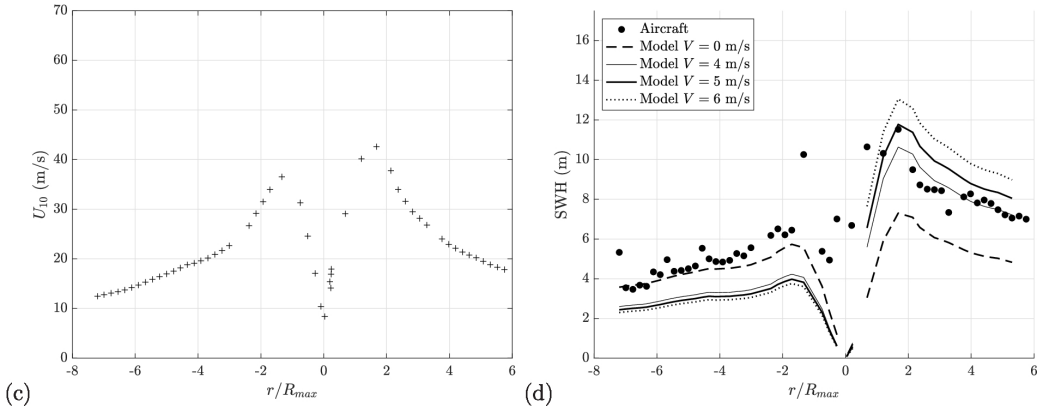

Figure 14: (a) ECMWF wind speed interpolated at the aircraft location, U_{10}. (b) SWH as measured by the aircraft (black dots) and estimated using the KGC15 model combined using U_{10} for $V = 0$ m·s^{-1} (dashed line), $V = 4$ m·s^{-1} (thin line), $V = 5$ m·s^{-1} (thick line) and $V = 6$ m·s^{-1} (dotted line). Abscissa: distance to the TC center (defined with the same sign as x) normalized by R_{max}.

front and left-rear quadrants of SAM on 30 September between 01:16 and 02:09. The SWH measured by the WSRA onboard the aircraft is compared to the modelled SWH, calculated using equation (9) in C and the ECMWF surface wind speed, U_{10}, interpolated along the aircraft trajectory (Figure 14a). The SWH profiles across SAM are shown in Figure 14b. If the TC is assumed to be stationary ($V = 0$), the SWH predicted by the KGC15 model strongly underestimates the SWH observed in the right-front sector (compare the black dots and the dashed line in Figure 14b), which suggests that the asymmetry of the wind alone can not explain the observed asymmetry in SWH. However, if values of V close to the IBTrACS estimate $V \simeq 5$ m·s^{-1} are used, the KGC15 model allows to retrieve the large SWH observed in the right front sector. That means that a trapped wave mechanism could be invoked to explain the SWH asymmetry. It is however important to keep in mind that the ECMWF wind might underestimate winds in SAM. Indeed, during the reconnaissance flight, the maximum recorded wind speed in the IBTrACS database is 64 m·s^{-1}, which suggests that the ECMWF winds shown in Figure 14a might be slightly underestimated. We therefore now turn to the *in situ* measurements (saildrone and buoy) in order to have collocated measurements of waves and wind at the surface.

This issue is thus finally addressed in Figure 15 using the *in situ* measurements by the SD and by the buoy 41044. Indeed, these two instruments provide measurements of wind and waves across the right quadrants of SAM, where the phenomenon of trapped waves is likely to occur, passing within a few tens of kilometers from its center (see insets in Figures 15a and 15c). The surface wind speed and SWH measured by the SD from 29 September 01:00 to 1st October 17:30 (resp. by the buoy 41044 from 28 September 10:40 to 1st October 10:40) are shown in Figure 15a (resp. Figure 15c), as a function of the distance to the TC center, r, defined as positive in the right-front quadrant and negative in the right-rear quadrant. The SWH as estimated by the KGC15 model using the *in situ* wind profiles as well as the propagation velocity V of SAM (shown in Figure 15b and Figure 15d) is superimposed in red in Figure 15a and Figure 15c. Setting $V = 0$ in the model yields the black curve. In both cases, the latter strongly underestimates the SWH, whereas taking account the motion of SAM yields values much closer to the SWH measurements. This implies that the large values of SWH observed in the right quadrants of SAM by the SD and by the buoy 41044 are consistent with the extended fetch theory. Note that the critical fetch defined in (8) for winds blowing at 40 $\mathrm{m{\cdot}s^{-1}}$ and a translation velocity $V = 7$ $\mathrm{m{\cdot}s^{-1}}$ (which is the value of V according to IBTrACS when both devices are closest to the center of SAM) is approximately 30 km. This corresponds to a distance of about 10 km from the axis. The SD and the buoy 41044 thus operate in regions where conditions are favorable for trapped waves. To put it further to the test, the group velocity C_g is calculated from the peak period T_p measured by both devices using the gravity waves dispersion relation. It is shown in Figure 15b and Figure 15d (see the black diamonds). It can be noticed that the group velocity measured by the SD exhibits more variability than that measured by the buoy, due to fluctuating values of T_p. In the KGC15 model, which involves a constant V, trapped waves are characterized by $C_g = V$ at the turning point, where waves change direction (from backward to forward), and by an increasing C_g as they move forward. This tendency is consistent with the increasing dominant wavelength as the SD and the buoy 41044 move forward to the front of SAM (Figure 3b). The propagation speed V of SAM during the time period investigated here keeps decreasing as r decreases (see the black crosses in Figures 15b and 15d). In order to get rid of this tendency, the ratio C_g/V is superimposed to the C_g and V profiles in Figures 15b and 15d (blue dots). The ratio C_g/V as measured by the SD (resp. by the buoy 41044) varies from 0.5 (resp. 1) to 2.5

as r increases, which is consistent with growing waves propagating forward. The region where C_g is approximately equal to V (compare the blue dots to the blue line indicating $C_g = V$ in Figures 15b and 15d) is located upstream of the region with the highest SWH (blue dots in Figures 15a and 15c), which is expected in the trapped wave phenomenon. The ratio C_g/V as predicted by the KGC15 model is superimposed (see the red curve in Figures 15b and 15d): it provides a good description of the C_g/V profile, which corroborates a wave trapping mechanism in the area explored by the SD and the buoy 41044.

6 Conclusions

The present paper takes advantage of the numerous observational data in Hurricane SAM (2021) from satellite, aircraft and *in situ* instruments, to investigate the physics of waves in Hurricane SAM. Whereas the SWIM wave measurements have been used in several previous studies to investigate waves in tropical cyclones, the relevance of the wave spectra in such heavy rain conditions has not been investigated so far. In the present study, we assess the reliability of SWIM measurements in TCs, by comparing the SWIM wave spectra, as well as the averaged parameters (SWH, dominant wavelengh, dominant direction), to that measured by 3 NDBC buoys and a saildrone (SD 1045) close to the track of Hurricane SAM. According to the spatial and temporal variability of waves in TCs, such a comparison makes sense only if the satellite and *situ* measurements are close enough, both in time and space, which strongly restricts the number of relevant comparisons. The case of Hurricane SAM, was thus complemented by 8 additional storms and hurricanes, for which collocated SWIM and NDBC measurements were performed in the vicinity of the storm, in various rain conditions, including heavy rain conditions. Those comparisons confirm the reliability of SWIM wave spectra, even in heavy rain conditions, despite a tendency for overestimating the energy at small k (more pronounced for SWH less than about 3 meters) in the presence or absence of rain (Jiang et al., 2022).

To understand why the SWIM spectra remain reliable in heavy rain conditions, we then focused on the post-processing chain of the SWIM instrument, from the radar backscattering signal to the 2D wave spectra, which are reconstructed by combining the measurements of wave energy propagating along footprints covering the angular range $[0, 180]^\circ$. We have shown that

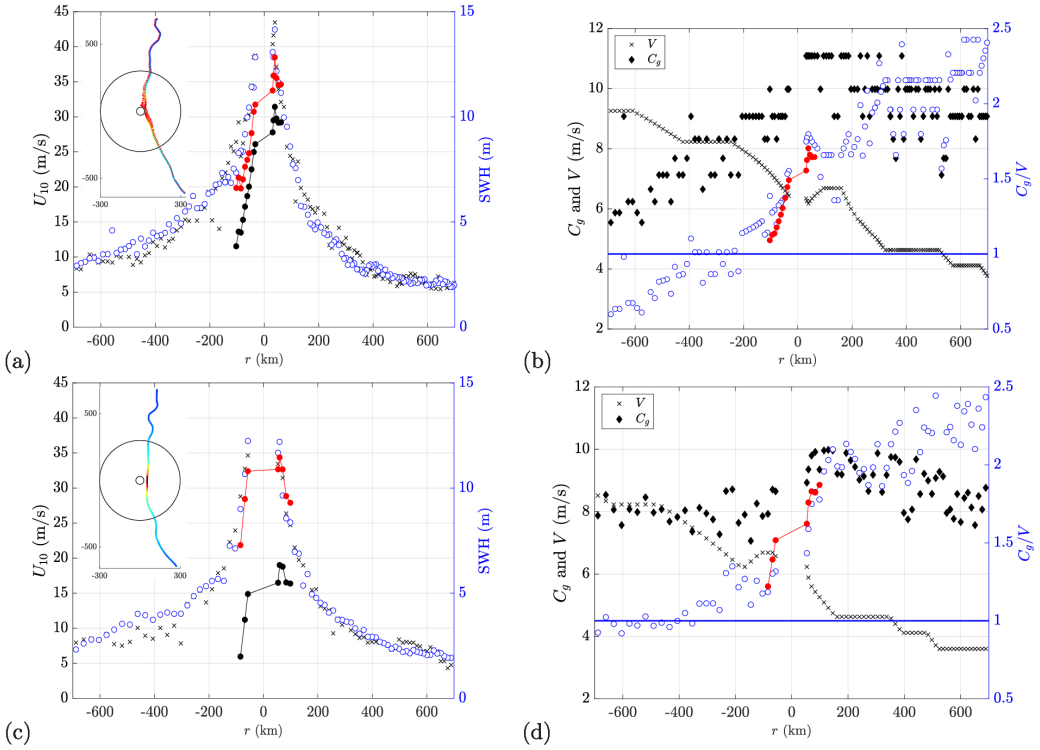

Figure 15: (a) Surface wind speed U_{10} (black crosses) and SWH measured by the SD (blue circles), superimposed to the SWH estimated by the KGC15 model using the translation velocity of SAM V (red line) or setting $V = 0$ m·s^{-1} (black line). (b) Group velocity C_g measured by the SD (black diamonds) and V (black crosses), superimposed to C_g/V (blue circles) and to its estimation by the KGC15 model (red line). Blue line indicates $C_g/V = 1$. (c) and (d): Same as (a) and (b) but for the buoy 41044. Abscissa: distance to the TC center (defined with the same sign as y). The trajectory in the frame of SAM of the SD and of the buoy 41044 (colored by the SWH and superimposed to the wind vectors) are shown on the insets in panels (a) and (c).

heavy rain yields an attenuation of the normalized radar cross section σ_0 and that in case of rain inhomogeneity along the footprints, the σ_0 signal is distorted, leading to an anomalous peak at small wavenumber (wavelengths larger than 1 km) in the modulation wave spectra. However, thanks to a filtering of both the values corresponding to a low signal-to-noise ratio and the energy at wavenumbers smaller than $k_{min} = 0.01$ m^{-1}, both effects do not affect the resulting 2D wave spectra.

We then investigated the existence of trapped waves in Hurricane SAM, using a combination of satellite, aircraft and *in situ* wind and wave measurements. To do so, we also used the analytical model of Kudryavtsev et al. (2015) which predicts the wave properties (SWH and peak wavelengh) in the right and left quadrants of a moving TC, given a surface wind speed profile. The model relies on the idea that in the right quadrants of TCs, some waves may experience an extended fetch due to the displacement of the TC. This reinforces the SWH asymmetry induced by the wind speed asymmetry and results in the highest waves on the right of the TC track in the North Hemisphere. Using the wind and wave measurements by a SD and a NDBC buoy through the right quadrants of hurricane SAM, we have shown that a trapped wave mechanism may be invoked to explain the large SWH measured by both devices in the right-front quadrant. It is also consistent with the aircraft measurements, although significant uncertainties remain regarding the ECMWF wind speed. Note that the orientation and the distance of the SWIM tracks through hurricane SAM were not optimal for comparisons with the model.

Beside the impressive images and movies provided by the saildrones in TCs, their wind and wave measurements can be very valuable to improve our understanding of the generation of waves in TCs. The same applies to the wave measurements by SWIM whose wave spectra have been shown, in the present study, to be reliable even under heavy rain conditions. With more saildrones being deployed, and as SWIM continues to operate, further hurricanes will be studied using the combined approach advocated in this paper and will most certainly improve our understanding of the most threatening waves under a tropical cyclone.

7 Open Research

The CFOSAT SWIM data are available on https://aviso-data-center.cnes.fr (L1A) and https://www.aviso.altimetry.fr/en/data/products/wind/wave-products/wave-wind-cfosat-products.html (L1B and L2). The SWIM L2S data are provided by the Ifremer Wind and Wave Operation Center on https://cersat.ifremer.fr/fr/Projects/Recent-and-ongoing-projects/IWWOC. The *in situ* data are available on the NOAA website: https://data.pmel.noaa.gov/pmel/erddap/tabledap/sd1045_hurricane_2021.html and https://www.ndbc.noaa.gov . The IBTrACS database can be downloaded from https://www.ncei.noaa.gov/products/international-best-track-archive-for-climate-stewardship-ibtracs/v04r00. The ECMWF wind data are available on the ECMWF's Meteorological Archival and Retrieval System (https://confluence.ecmwf.int/display/CEMS/MARS). Finally, the GPM IMERG precipitation data can be downloaded from NASA https://gpm.nasa.gov/data/directory.

Acknowledgments

This work was performed during a research visit of Xiaolu Zhao in Sorbonne Université from April 2022 to April 2024. This visit was supported in part by the China Scholarship Council (CSC) Ph.D. Joint Training Program under Grant #202109040021. This research project is partly supported by the CNES/TOSCA (Maeva project). We thank the NOAA and the Saildrone company for sharing the saildrone data.

A SAR performances

On 2 and 3 October 2021, the SWIM-CFOSAT and SAR-Sentinel1 instruments passed closed to each other (SWIM boxes and SAR imagettes being located at less than 40 km) in the rainbands of SAM with an approximate time-lapse of about 1h30. Figure 16 shows a first example of collocated SWIM and SAR wave height spectra on 2 October. Their locations are highligted by the red and purple rectangles in Figure 16a, superimposed to the rain rate field: in this example no rain is detected within the SWIM box and the SAR imagette. The SAR SWH is a factor 1.5 smaller than the SWIM nadir SWH, and the SAR detects much less energy than SWIM at wavenumbers larger than 0.03 m^{-1} (i.e. wavelenghs smaller than 160 m): this attenuation is characteristic of the cut-off effect. A second comparison, this time under moderate rain, is carried out in Figure 17. In this case, the rain rate reaches 3.4 mm/hr in the SWIM box and 3.2 mm/hr in the SAR imagette. The SAR SWH is smaller by a factor 2.5 compared to the SWIM nadir SWH and the SAR spectrum is strongly attenuated over the entire wavenumber range, compared to SWIM. Since the waves propagate in a direction closer to the range direction than to the azimuth direction, the cut-off effect can not explain such a discrepancy between both spectra and the latter is more likely due to rain.

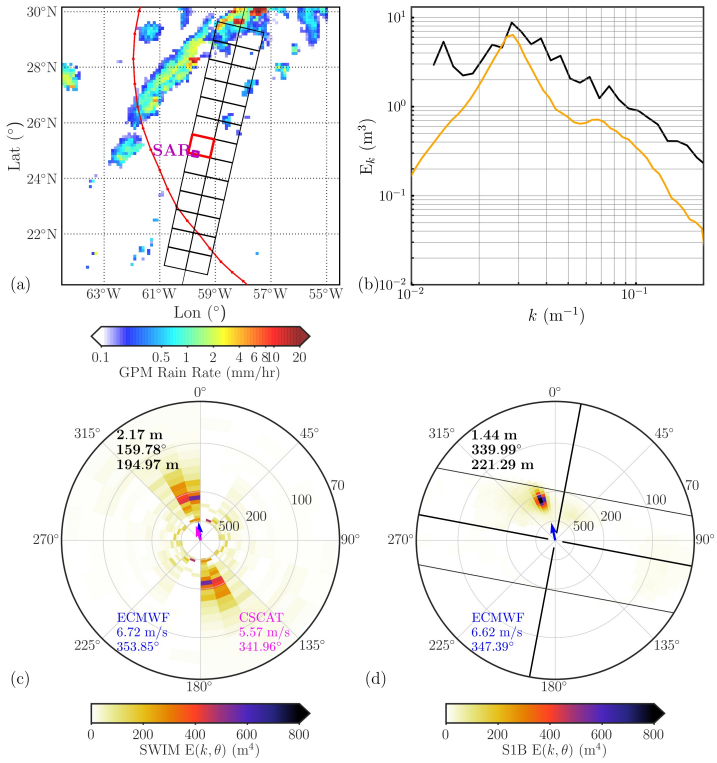

Figure 16: (a) SWIM boxes (black quadrangles) and SAR imagette (in purple) superimposed to the rain rate field in mm/hr (in colors); red line: the best track of the storm; red cross: storm center during the passage of SWIM. (b) SWIM (black) and SAR (orange) 1D wave height spectra corresponding to the SWIM box highlighted in red in (a) and to the SAR imagette. Corresponding (c) SWIM and (d) SAR 2D wave height spectra; thick solid lines: azimuth and range directions, thin solid line: shortest detectable wavelengths.

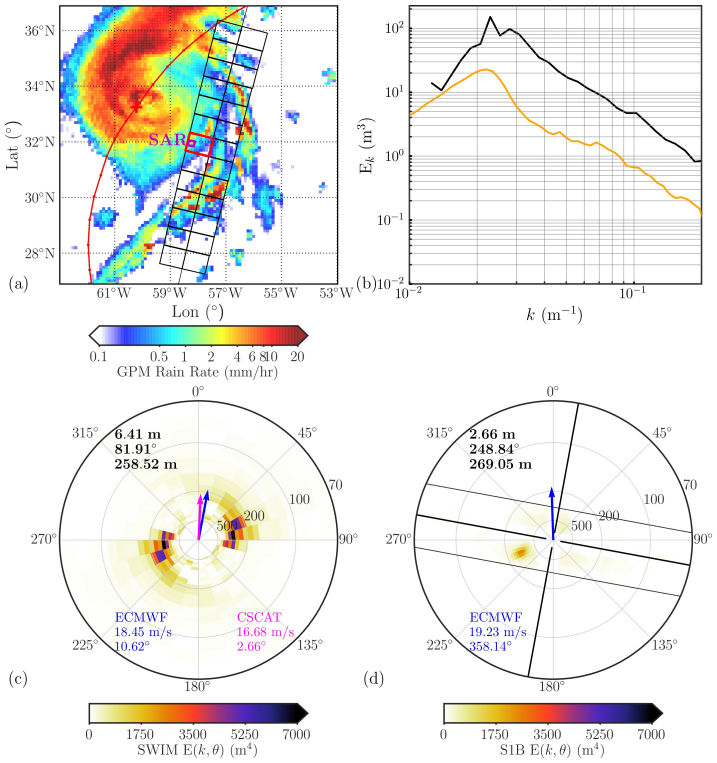

Figure 17: Same as Figure 16 but corresponding to SWIM boxes and SAR imagette under moderate rain conditions.

B Statistical study of the rain impact on modulation wave spectra

Beyond the SWIM measurements along the 3 footprints shown in Figures 9, 10 and 11, the measurements within the footprints within 350 km from the TC center during the passage of SWIM on 1st October 2021 are now investigated.

Figure 18 shows the averaged value of the reliable σ_0 profiles ($\overline{\sigma_0}$) as a function of the collocated rain rate (RR) estimated at the middle of the footprints, for the 3 spectral beams. It highlights the attenuation of $\overline{\sigma_0}$ by rain. For a RR of 10 mm/hr, it reaches up to 6 dB for the 10° beam. The spatial resolution of the IMERG product (about 10 km) is unfortunately too low for quantifying the rain inhomogeneities along the footprints (about 20 km length). The following figures thus involve the rain rate at the middle of the footprints. Figure 19a shows the large-scale variability of σ_0 within the footprints of the 10° spectral beam (quantified by the $lsvar$ parameter) as a function of the rain rate RR. For moderate and heavy rains, there is a correlation between $lsvar$ and RR. The representation of the averaged value of $lsvar$ per rain rate category in Figure 19c corroborates the correlation between both quantities when RR is larger than 7 mm/hr. The energy of the small k peak on the modulation spectra is quantified by

$$\mathcal{E}_{k<k_c} = \int_{k<k_c} \mathrm{Pm}(k) dk \,, \tag{5}$$

where $k_c = 2\pi \cdot 10^{-3}$ m^{-1} (i.e. $\lambda_c = 1$ km). This quantity corresponds to the energy of the modulation spectra at wavelengths larger than 1 km. This threshold value was chosen in order to distinguish the small k anomalous peak to the ocean wave spectrum. Figure 19b shows $\mathcal{E}_{k<k_c}$ as a function of RR, whereas its averaged value per rain rate category is represented in Figure 19d. These figures highlight the correlation of $\mathcal{E}_{k<k_c}$ with RR for moderate and heavy rains. Actually, the rain rate at the middle of the footprint is not necessarily correlated to the rain inhomogeneities along the footprint. For example, the rain rate in case 3 (Figure 11) is larger than that in case 2 (Figure 10). Yet, the σ_0 signal is more distorted in case 2, suggesting that rain inhomogeneities are more important in case 2. This can explain why the correlations shown in Figure 19 are not stronger. The rain product spatial resolution (about 10 km) is definitely a limiting factor in the investigation

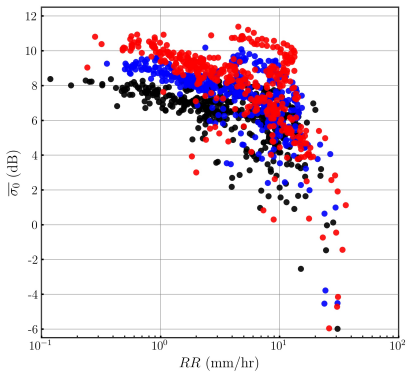

Figure 18: Averaged value of the reliable σ_0 profile ($\overline{\sigma_0}$) as a function of the collocated rain rate (RR) estimated at the middle of the 405 footprints of the 6° beam (red color) and 407 footprints of the 8° (blue color) and 10° (black color) beams.

of the impact of rain inhomogeneities on SWIM measurements. This is also the case for its half-hourly temporal resolution.

The investigation of the rain impact on the rest of the modulation spectrum (i.e. for $k > k_c$), including the waves energy, deserves a slightly different methodology, relying on both 8° and 10° spectral beams. Indeed, since this part of the modulation spectrum contains the waves energy, the rain impact can be assessed only by comparing measurements of the same waves but in different rain conditions. The idea is to compare modulation spectra derived from 8° and 10° beams corresponding to very close azimuth directions, thus measuring waves propagating in the same direction. Assuming that the distance between both footprints is smaller than the spatial variability of waves, but is larger than the spatial variability of the rain field, the discrepancy between both measurements can be assumed to be due to the rain impact. As an example, the footprints of the 10° beam (resp. 8° beam) corresponding to the box 78-1 are superimposed to the rain rate field in Figure 20a (resp. 20b): whereas they are 22 km apart, the footprint number 3 of beam 10° in the azimuth direction 166° (Figure 20a) undergoes less rain ($RR \approx 2$ mm/hr) than the footprint number 4 of beam 8° in the very close azimuth direction 163° ($RR > 7$ mm/hr).

A comparison of the modulation spectra as measured within footprints corresponding to 10° and 8° beams in very close azimuth directions was un-

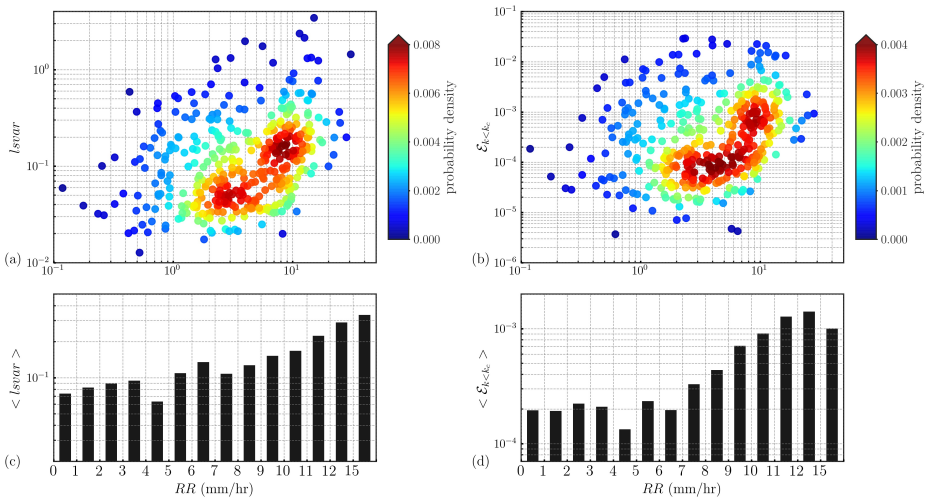

Figure 19: Scatterplot and probability density function (colors) of (a) the large-scale variability within the footprints ($lsvar$) and of (b) the energy $\mathcal{E}_{k<k_c}$, as a function of the rain rate RR at the middle of the 407 footprints of the 10° spectral beam. Corresponding averaged values of (c) $lsvar$ and of (d) $\mathcal{E}_{k<k_c}$ per category of RR.

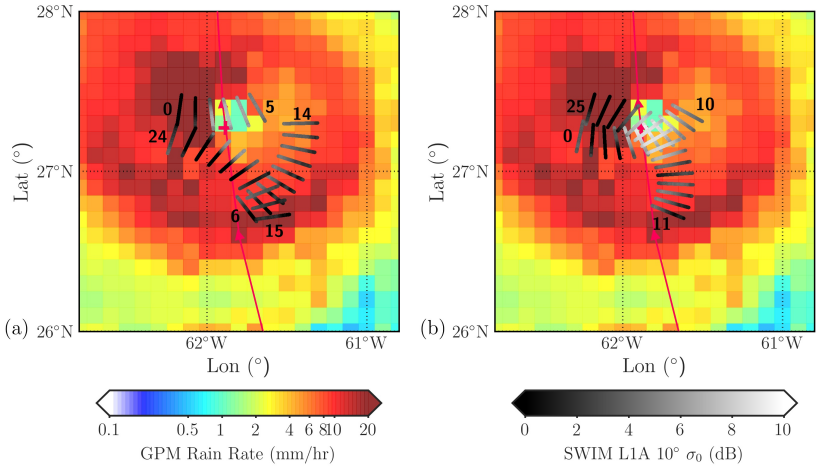

Figure 20: Footprints corresponding to the (a) 10° and (b) 8° beams, in the box 78-1, superimposed to the rain rate field (in colors) on 1st October 11:30. Red line: trajectory of the center of SAM. Red cross: location of the center of SAM during the passage of SWIM.

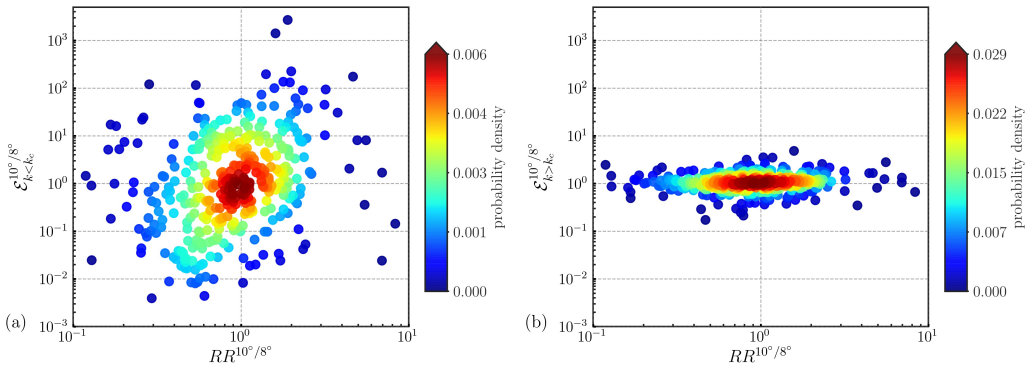

Figure 21: Scatterplot and probability density function (colors) of (a) $\mathcal{E}_{k<k_c}^{10/8^\circ}$ and (b) $\mathcal{E}_{k>k_c}^{10/8^\circ}$ as a function of $RR^{10/8^\circ}$, for 391 comparisons.

dertaken, related to the rain rates. Among the 391 comparisons, the distance between both footprints varies from 20 km to 53 km and the azimuth direction difference from 1.15° to 4.30°. Note that this methodology implies an estimation of rain at the middle of both footprints: hence, the limitations due to the spatial and temporal resolutions of the rain product are now twice as critical compared to Figure 19. Figure 21a shows the ratio of $\mathcal{E}_{k<k_c}$ as measured at 10° to that at 8° (such a ratio is denoted as $\mathcal{E}_{k<k_c}^{10/8^\circ}$), as a function of the ratio of rain rates, denoted as $RR^{10/8^\circ}$. Despite scattered data, this figure exhibits a correlation between both quantities, which is consistent with Figure 19b. Such a correlation is not observed between $\mathcal{E}_{k>k_c}^{10/8^\circ}$ and $RR^{10/8^\circ}$, as shown in Figure 21b. This suggests that rain mainly impacts the modulation spectra at small wavenumbers ($k < k_c$), rather than the waves range.

C KGC15 model for trapped waves

The KGC15 model aims at predicting the waves properties of the strongest waves at a given location in the right and left quadrants of a TC using the wind speed u_w and the translation speed of the TC, V. The wind speed is supposed to be parallel to the TC axis and uniform along this direction and waves are supposed to propagate along the same direction. In a stationary TC, the inverse wave age α_0 (defined as u_w/C_p, where C_p is the phase velocity of the wave) and the dimensionless energy of waves $\tilde{\mathrm{E}}_0$ (using u_w^4/g^2 as unit of energy) are estimated as

$$\alpha_0 = c_\alpha \tilde{\mathrm{X}}^q \qquad \text{and} \qquad \tilde{\mathrm{E}}_0 = c_e \tilde{\mathrm{X}}^p \,, \tag{6}$$

where $\tilde{\mathrm{X}}$ is the dimensionless fetch length (using u_w^2/g as unit of length), measured as the distance from the $y = -ax$ reference line ($\tilde{\mathrm{X}}$ is defined as a positive quantity in both quadrants). In Kudryavtsev et al. (2015), $a = 1$ (that corresponds to a 45° angle); a slightly larger value is chosen here ($a = 1.37$, corresponding to a 54° angle), in order to extend slightly the range of applicability of the model and thus get more comparisons with observational data. Following Kudryavtsev et al. (2015), the fetch law exponents p and q are chosen as $p = 0.89$ and $q = -0.275$, which yields $c_\alpha = 15.14$ and $c_e = 4.41 \times 10^{-7}$. According to (6), a symmetrical wind field yields a symmetrical wave field. The symmetry is broken in a moving TC, where the inverse wave age obeys

$$\begin{cases} \alpha^{1/q} \left[1 - (1+q)^{-1} \alpha/\alpha_T\right] = c_\alpha^{1/q} \left[\tilde{\mathrm{X}} - \tilde{\mathrm{L}}_{cr}\right] & \text{if} \quad x > 0 \text{ and } \tilde{\ell} > \tilde{\mathrm{L}}_{cr} \,, \\ \alpha^{1/q} \left[1 - (1+q)^{-1} \alpha/\alpha_T\right] = c_\alpha^{1/q} \left[\tilde{\mathrm{X}} - \tilde{\ell}\right] & \text{if} \quad x > 0 \text{ and } \tilde{\ell} < \tilde{\mathrm{L}}_{cr} \,, \\ \alpha^{1/q} \left[1 + (1+q)^{-1} \alpha/\alpha_T\right] = c_\alpha^{1/q} \tilde{\mathrm{X}} & \text{if} \quad x < 0 \,, \end{cases} \tag{7}$$

where $\tilde{l}$ is the dimensionless length of the segment between the $y = ax$ and $y = -ax$ lines and $\tilde{\mathrm{L}}_{cr}$ is the dimensionless critical fetch defined as

$$\tilde{\mathrm{L}}_{cr} = -c_\alpha^{-1/q} \frac{q}{1+q} \alpha_T^{1/q} \,, \tag{8}$$

$\alpha_T = u_w/(2V)$ being the inverse wave age when their group velocity equals the TC propagation speed V. The energy $\tilde{\mathrm{E}}$ is deduced from (7) through

$$\tilde{\mathrm{E}} = c_e \left(\alpha/c_\alpha\right)^{p/q} \,. \tag{9}$$

If $\tilde{l} > \tilde{\mathrm{L}}_{cr}$, waves generated in the right quadrants first travel backward in the frame of the TC, their group velocity increasing until reaching V at a so-called turning point ($\alpha = \alpha_T$), after which they start to propagate forward increasing their group velocity ($\alpha < \alpha_T$) until leaving the TC. These waves have an extended fetch $\tilde{\mathrm{X}} + \tilde{\mathrm{L}}_{cr}$. If $\tilde{l} < \tilde{\mathrm{L}}_{cr}$, the waves never reach a group velocity matching V and propagate backward. Finally, in the left quadrants, where the TC propagation is opposite to the TC winds, the waves propagate backward and have a reduced fetch compared to the stationary case. In the model, the TC forcing conditions (wind speed and propagation velocity) are supposed to be constant while the waves are propagating in the TC. The above relations are thus relevant if the TC is quasi-stationary during the time-period T, this yields an upper bound on the fetch duration

$$\mathrm{T} \leq \frac{u_w}{g} \frac{2c_\alpha}{1+q} \left(2\,\tilde{\ell}\right)^{1+q} . \tag{10}$$

In the case of hurricane SAM, at a distance corresponding to $R_{max} = 28$ km and using $u_w = 40$ m/s, (10) the model thus assumes steady winds and a constant translation velocity over a time $\mathrm{T} \leq 6.8$ hours.

References

Alpers, W., Zhang, d. M. A., B. a, Zeng, K., & Chan, P. W. (2016). Rain footprints on c-band synthetic aperture radar images of the ocean - revisited. *Remote Sensing of Environment*, *187*, 169–185.

Badulin, S. I., Babanin, A. V., Zakharov, V. E., & Resio, D. (2007). Weakly turbulent laws of wind-wave growth. *J. Fluid. Mech.*, *591*, 339–378.

Bidlot, J.-R., Prates, F., Ribas, R., Mueller-Quintino, A., Crepulja, M., & Vitart, F. (2020). Enhancing tropical cyclone wind forecasts. *ECMWF Newsletter*, *164*, 33–37.

Bowyer, P., & MacAfee, A. W. (2005). The theory of trapped-fetch waves with tropical cyclonesan operational perspective. *Weather forecast.*, *20*, 229–244.

Hauser, D., Abdalla, S., Ardhuin, F., Bidlot, J.-R., Bourassa, M., Cotton, D., Gommenginger, C., Evers-King, H., Johnsen, H., Knaff, J., Lavender,

S., Mouche, A., Reul, N., Sampson, C., Steele, E., & Stoffelen, A. (2023). Satellite remote sensing of surface winds, waves, and currents: Where are we now? *Surv. Geophys.*, *44*, 1357–1446.

Hauser, D., Tourain, C., Hermozo, L., Alraddawi, D., Aouf, L., Chapron, B., Dalphinet, A., L, D., Dalila, M., Dormy, E., Gouillon, F., Gressani, V., Grouazel, A., Guitton, G., Husson, R., Mironov, A., Mouche, A., Ollivier, A., Oruba, L., Piras, E., Suquet, R. R., Schippers, P., Tison, C., & Tran, N. (2021). New observations from the swim radar on board cfosat: Instrument validation and ocean wave measurement assessment. *IEEE Trans. Geosci. Remote Sens.*, *1*, 05–26.

Huffman, G., Stocker, E., Bolvin, D. T., Nelkin, E. J., & Tan, J. (2023). Gpm imerg final precipitation l3 half hourly 0.1 degree x 0.1 degree v07. *Greenbelt, MD, Goddard Earth Sciences Data and Information Services Center (GES DISC), Accessed: [Data Access Date], 10.5067/GPM/IMERG/3B-HH/07*.

Jiang, H., Song, Y., Mironov, A., Yang, Z., Xu, Y., & Liu, J. (2022). Accurate mean wave period from swim instrument on-board cfosat. *Remote Sensing of Environment*, *280*, 113149.

Kudryavtsev, V., Golubkin, P., & Chapron, B. (2015). A simplified wave enhancement criterion for moving extreme events. *J. Geophys. Res. Oceans*, *120(11)*, 7538–7558.

Kudryavtsev, V., Yurovskaya, M., & Chapron, B. (2021a). 2d parametric model for surface wave development under varying wind field in space and time. *J. Geophys. Res. Oceans*, *126*(e2020JC016915).

Kudryavtsev, V., Yurovskaya, M., & Chapron, B. (2021b). Self-similarity of surface wave developments under tropical cyclones. *J. Geophys. Res. Oceans*, *126*, e2020JC016916.

Le Merle, E., Hauser, D., & Yang, C. (2022). Wave field properties in tropical cyclones from the spectral observation of the cfosat/swim spaceborne instrument. *Geophys. Res. Lett.*, *128*(e2022JC019074).

Li, D., Staneva, J., Bidlot, J.-R., Grayek, S., Zhu, Y., & Yin, B. (2021). Improving regional model skills during typhoon events: A case study for

super typhoon lingling over the northwest pacific ocean. *Front. Mar. Sci.*, *8*(613913).

Lygre, A., & Krogstad, H. E. (1986). Maximum entropy estimation of the directional distribution in ocean wave spectra. *J. Phys. Oceanogr.*, *16*, 2052–2060.

Oruba, L., Hauser, D., Planes, S., & Dormy, E. (2022). Ocean waves in the south pacific: Complementarity of swim and sar observations. *Earth Space Sci.*, *9*.

Quilfen, Y., Chapron, B., & Tournadre, J. (2010). Satellite microwave surface observations in tropical cyclones. *Mon. Weather Rev.*, *111*(C01004).

Quilfen, Y., Tournadre, J., & Chapron, B. (2006). Altimeter dual-frequency observations of surface winds, waves, and rain rate in tropical cyclone isabel. *J. Geophys. Res.: Oceans*, *111*(C01004).

Ricciardulli, L., Foltz, G., Manaster, A., & Meissner, T. (2022). Assessment of saildrone extreme wind measurements in hurricane sam using mw satellite sensors. *Remote Sens.*, *14*, 2726.

Shi, Y., Du, Y., Chu, X., Tang, S., Shi, P., & Jiang, X. (2021). Asymmetric wave distributions of tropical cyclones based on cfosat observations. *J. Geophys. Res. Oceans*, *126*.

Welch, P. D. (1967). The use of fast fourier transforms for the estimation of power spectra: A method based on time averaging over short modified periodograms. *IEEE Transactions on Audio and Electroacoustics*, *15*, 70–73.

Xiang, K., Yin, X., Xing, S., Kong, F., Li, Y., Lang, S., & Gao, Z. (2022). Preliminary estimate of cfosat satellite products in tropical cyclones. *IEEE Trans. Geosci. Remote Sens.*, *60*(4203516).

Young, I. R. (1988). Parametric hurricane wave prediction model. *J. Waterw. Port, Coast. Ocean Eng.*, *114*(5), 637–652.

Young, I. R. (2017). A review of parametric descriptions of tropical cyclone wind-wave generation. *Atmosphere*, *8*(194), 1–20.

Yurovskaya, M., Kudryavtsev, V., Mironov, A., Mouche, A., Collard, F., & Chapron, B. (2022). Surface wave developments under tropical cyclone goni (2020): Multi-satellite observations and parametric model comparisons. *Remote Sens.*, *14*(2032).

Zhao, X., Lin, W., Portabella, M., Wang, Z., & He, Y. (2022). Effects of rain on cfosat scatterometer measurements. *Remote Sens. Environ.*, *274*, 113015.

Zhao, X., Shao, W., Zhao, L., Gao, Y., Hub, Y. Y., & Yuan, X. (2021). Impact of rain on wave retrieval from sentinel-1 synthetic aperture radar images in tropical cyclones. *Adv. Space Res.*, *67*, 3072–3086.

Zieger, S., Inoth, J. V., & Young (2009). Joint calibration of multiplatform altimeter measurements of wind speed and wave height over the past 20 years. *J. Atmos. Ocean. Technol.*, *26*, 2549–2564.